

# Selection of axial dipole from a seed magnetic field in rapidly rotating dynamo models

Subhajit Kar

---

## Abstract

In this study, we investigate preferences of dipolar magnetic structure from a seed magnetic field in the rapidly rotating spherical shell dynamo models. In this study, we set up a realistic model to show the effect of the Lorentz force in the polarity selection. The important results that has come out from our study is that the magnetic field acts on the flow much before the saturation. Our study suggests that the growth of the magnetic field is not a kinematic effect as one might think off, rather a dynamic effect. This dynamic effect grows as the field generated with time and finally brings the saturation to the dynamo action. Previous studies show that Lorentz force effect the flow when Elsasser number more or less 1 and the studies were focused on the saturation by looking at the time-averaged quantities. However, in this study, we show a clear effect of the Lorentz force even at Elsasser number of  $0.3 - 0.4$ . To show the effect of the Lorentz force, we did two different simulations, one is a nonlinear model and another is kinematic model and shows that how a magnetic field can change the flow structure and by doing that the generated field changes, while this kind of behavior is not observed in kinematic dynamo models. This study shows a scale dependent behaviour of the kinetic helicity at two different spectral range.

*Keywords:* `elsarticle.cls`, L<sup>A</sup>T<sub>E</sub>X, Elsevier, template

*2010 MSC:* 00-01, 99-00

---

## 1. Introduction

The generation of magnetic field inside a rapidly rotating planetary core is a fundamental problem in geophysics. There has been considerable progress in modelling convection in rapidly rotating spherical shells, and the dynamo action; see for example

the recent reviews [1] , [2]. It is widely believed that the fluid in planetary cores is stirred by the columnar convection under rapid rotation which transports the heat from deep core to outer boundary, though precessional effects may also be involved in magnetic field production. It is suggested that magnetic field of earth is maintained by thermal as well as compositional convection though latter is most dominant. However, the convection driven dynamos shows different types magnetic field structure can be generated - axial dipole, quadrupole [3] [4] [5], or even equatorial dipole [6] [7]. However, axial dipole structure is very common in rapidly rotating dynamos, where the inertia (nonlinear part of the advection) in the equation of motion is very small. Estimates of the core flow velocity (see, [8]) suggest that inertia is significant in planetary cores at length scales so small that magnetic diffusion is very rapid, so the expected regime is indeed where axial dipole dominance is found. This may explain why most planetary dynamos are approximately dipolar, the only exceptions being Uranus and Neptune, whose physical properties are poorly understood. Though Earth lies in a rapidly rotating system. Magnetic field structure from observation at core-mantle boundary (CMB) suggests that it is dipole. Magnetic field structure from observation at core-mantle boundary (CMB) suggests that it is dipole. Most of the numerical simulations achieved dipole field as most dominant. But, the question arises why this structure is the most likely solution from spherical dynamo models. One way to study it is by having a flow field which can closely mimic the features (like - differential rotation, meridional circulations) of a rotating systems and see whether the dipole solution is favorable than any other solutions. But this approach is a linear, where back reaction of the magnetic field on flow is neglected. But in a planetary core, the effect of back reaction is important and therefore, study with a linear approach is incomplete. In this study we will show how back reaction can alter the growth of magnetic field and also its structure.

In a recent study by Schaeffer et al. [9], the authors have used using quasi-geostrophic formulation where,  $z$ -vorticity equation is computed at equatorial plane and extrapolated to the full sphere whereas, induction equation is solved in full sphere. Since, it

is a quasi-geostrophic model, so  $u_s$  and  $u_\phi$  are constant along the direction of rotation (independent of  $z$ ). This dynamo model excited Stewartson layer by rotating the polar cap (the imaginary cylinder of radius of inner core touches the outer boundary) at different rotation than the outside. So, it will generate a geostrophic shear layer adjacent to the tangent cylinder. Certainly, this low  $Pm$  models will have different characteristics than the usual convective dynamo models where geostrophic has to break down by convection itself though it will maintain the same velocity symmetry about the equator as dynamo models at close to onset of convection. The forcing of dynamo is defined by a non-dimensional quantity called Rossby number ( $Ro = \frac{\Delta\Omega}{\Omega}$ ), where  $\Delta\Omega$  is the differential rotation rate of the inner core. Above a critical value of  $Ro$  the Stewartson layer will become unstable and generate Rossby waves. In this dynamo models both symmetry of magnetic fields exist (namely, dipole and quadrupole). The authors noted that in this configuration the quadrupole family has lesser critical magnetic Reynolds number than the dipole to excite. Though their energy spectrum suggested that toroidal magnetic energy is more dominant than poloidal magnetic energy (about four orders of magnitude difference). It is an  $\alpha$ - $\omega$  dynamo model, where the shear inside the Stewartson layer will produce toroidal field from poloidal component, which is famously known as  $\omega$  effect whereas, the vortices produced by the Rossby waves will help to generate the poloidal field from the toroidal component (known as  $\alpha$  effect) and this is how the dynamo regeneration cycle will be completed. But a steady flow fails to produce any dynamo (kinematic) actions because in this scenario there is no Rossby waves and hence, the dynamo regeneration cycle will be stopped.

In a study by Aubert et al.[7], the authors have shown a self-consistent numerical dynamo models where both axial and equatorial dipoles can exist in a parameters regime of intermediate shell thickness (thickness ratio  $\geq 0.5$ ) and close to onset of convection. Their numerical simulations suggest that at close to onset of convection, equatorial dipole is favored whereas at slightly supercritical convection the field is dominated axial dipole. Also they have shown that once the strong axial dipole is setup, it is very difficult to kill it off by decreasing the Rayleigh number, which is

known as subcritical behaviour of dynamo. Most of their runs are at shell thickness ratio of greater than 0.5. They found that the equatorial dynamo solutions exist only at intermediate shell thickness ratio (0.45 - 0.7) but their strength is very low compared to the axial dipole.

Generation of magnetic field by convective dynamo models in a spherical shell were studied in case of Prandtl number of order one and a broad range of magnetic Prandtl number [4]. The authors find regular and chaotic dipolar dynamos, quadrupolar dynamos and hemispherical dynamos at different range of magnetic Prandtl number. The basic state temperature contains a uniform heat source and velocity boundary condition is stress-free on both sides of the spherical shell. The non-dimensional parameters are -  $Ek = 10^{-4}$ ,  $Pr = 1$ . They found that quadrupolar dynamos are preferred at  $Pm$  of order one while hemispherical dynamos are most at  $Pm$  of order 10.

Kinematic models help to find out what kind of flow structures can allow to have a dynamo action. Several people have tried to demonstrate the dynamo action with simplified flow structure which can mimic the flow of a rotating sphere (main features are - differential rotation, meridional circulations etc). One of the most cherished flow structure is Kumar-Roberts flow (in short KR flow). This flow contains differential rotation ( $T_1^0$ ), meridional circulation ( $P_2^0$ ) and two convective rolls ( $P_2^{2c}$  and  $P_2^{2s}$ ). In this paper, the authors explain the dynamo action by varying the above flow features by solving induction equation as eigenvalue problem where, magnetic Reynolds number ( $Rm$ ) is taken as eigenvalue. Lower value of  $Rm$  represents the ease of dynamo action. To get the confidence of their numerical convergence, the authors tried the solution near to Braginsky limit ( $Rm \rightarrow \infty$ ) by having strong axisymmetric differential rotation and small amount of meridional circulation and they found that differential rotation promotes axisymmetric toroidal field, whereas meridional circulation helps to generate axisymmetric poloidal field. They also found that non-axisymmetric helicity helps dynamo action by reducing critical  $Rm$ .

## 2. Numerical method

We consider an electrically conducting fluid confined in a spherical shell rotating with a constant angular velocity around  $z$ -axis. The radius of inner and outer spherical surfaces are  $r_i, r_o$  respectively, and ratio is chosen to be Earth like, 0.35. The governing equations considered are in the Boussinesq approximation. Lengths are scaled by thickness of the spherical shell  $L$ , and time is scaled by the magnetic diffusion time  $(t_d), (L^2/\eta)$ , where,  $\eta$  is magnetic diffusivity. The velocity field  $\mathbf{u}$  is scaled by  $\eta/L$ , and the magnetic field  $\mathbf{B}$  is scaled by  $(2\Omega\rho\mu\eta)^{1/2}$ , where  $\Omega$  is the rotation rate,  $\rho$  is the fluid density and  $\mu$  is the free space magnetic permeability.

The non-dimensional magnetohydrodynamic(MHD) equations for velocity, temperature and magnetic fields are

$$EPm^{-1}\left(\frac{\partial\mathbf{u}}{\partial t} + (\nabla \times \mathbf{u}) \times \mathbf{u}\right) + \hat{\mathbf{z}} \times \mathbf{u} = -\nabla p^* + qRaT\mathbf{r} + (\nabla \times \mathbf{B}) \times \mathbf{B} + E\nabla^2\mathbf{u} \quad (1)$$

$$\frac{\partial T}{\partial t} + \mathbf{u} \cdot \nabla T = q\nabla^2 T \quad (2)$$

$$\frac{\partial \mathbf{B}}{\partial t} = \nabla \times (\mathbf{u} \times \mathbf{B}) + \nabla^2 \mathbf{B} \quad (3)$$

$$\nabla \cdot \mathbf{u} = \nabla \cdot \mathbf{B} = 0 \quad (4)$$

The  $\nabla p^*$  in Eq. 1 is a modified pressure given by  $p + \frac{1}{2}EPm^{-1}|\mathbf{u}|^2$ , where  $p$  is the fluid pressure. The dimensionless parameters in Eqs. 1 - 3 are the Ekman number,  $E = \nu/2\Omega L^2$ , that measures the ratio of viscous to rotational forces, the Prandtl number,  $Pr = \nu/\kappa$  that gives the ratio of viscous to thermal diffusivities, the magnetic Prandtl number,  $Pm = \nu/\eta$  that gives the ratio of viscous to magnetic diffusivities and the 'modified' Rayleigh number (product of classical Rayleigh number and Ekman number) is given by  $g_o\alpha\Delta TL/2\Omega\kappa$ , where  $g_o$  is the gravitational acceleration acting

in radially inward,  $\alpha$  is the coefficient of thermal expansion,  $\Delta T$  is the superadiabatic temperature difference between boundaries and  $\kappa$  is the thermal diffusivity. The basic-state non-dimensional temperature distribution is a conventional basal heating  $T_o(r) = \beta/r$ , where  $\beta = r_i r_o$ . The velocity, temperature and magnetic fields satisfy the no-slip, isothermal and electrically insulating conditions, respectively. In order to characterize the results of the simulations, kinetic energy ( $E_k$ ), magnetic energy ( $E_m$ ) and Elsasser number ( $\Lambda$ ) are,

$$E_k = \frac{1}{2} \int_V |\mathbf{u}|^2 dV, \quad E_m = \frac{Pm}{2E} \int_V |\mathbf{B}|^2 dV, \quad \Lambda = \sqrt{\frac{2PmE_m}{EV}}. \quad (5)$$

where,  $V$  represents volume of the spherical shell.

The non-dimensional equations are solved using a pseudospectral method in which the velocity and magnetic field are expanded as toroidal and poloidal vectors, for example the toroidal-poloidal decomposition of velocity field is written as [10]

$$\mathbf{u} = \sum_{m=0}^M \sum_{l=1}^L (\mathbf{u}_{lm}^T + \mathbf{u}_{lm}^P) \quad (6)$$

where, superscripts  $T$  and  $P$  denotes toroidal and poloidal parts of  $\mathbf{u}$  at a given degree  $l$  and order  $m$ , respectively. Similar way we can expand magnetic field ( $\mathbf{B}$ ).

### 2.1. Equation of magnetic energy

The induction term of Eq. 2 can be rewritten in terms of toroidal and poloidal forms of velocity and magnetic field -

$$\begin{aligned} \frac{\partial \mathbf{B}}{\partial t} = & \left( \nabla \times (\mathbf{u}^P \times \mathbf{B}^P) + \nabla \times (\mathbf{u}^P \times \mathbf{B}^T) + \nabla \times (\mathbf{u}^T \times \mathbf{B}^P) + \right. \\ & \left. \nabla \times (\mathbf{u}^T \times \mathbf{B}^T) \right) + \nabla^2 \mathbf{B} \end{aligned} \quad (7)$$

The magnetic energy equation integrating over spherical shell volume ( $V$ )

$$\begin{aligned} \frac{Pm}{2E} \frac{d}{dt} \int_V |\mathbf{B}|^2 dV = & \frac{Pm}{E} \int_V \mathbf{B} \cdot \left( \nabla \times (\mathbf{u}^P \times \mathbf{B}^P) + \nabla \times (\mathbf{u}^P \times \mathbf{B}^T) + \right. \\ & \left. \nabla \times (\mathbf{u}^T \times \mathbf{B}^P) + \nabla \times (\mathbf{u}^T \times \mathbf{B}^T) \right) dV + \frac{Pm}{E} \int_V \mathbf{B} \cdot \nabla^2 \mathbf{B} dV \end{aligned} \quad (8)$$

Therefore, the energy equation for  $\mathbf{B}_{20}^T$  becomes

$$\begin{aligned} \frac{Pm}{2E} \frac{d}{dt} \int_V |\mathbf{B}_{20}^T|^2 dV = \frac{Pm}{E} \int_V \mathbf{B}_{20}^T \cdot \left( \nabla \times (\mathbf{u}^P \times \mathbf{B}^P) + \nabla \times (\mathbf{u}^P \times \mathbf{B}^T) + \right. \\ \left. \nabla \times (\mathbf{u}^T \times \mathbf{B}^P) + \nabla \times (\mathbf{u}^T \times \mathbf{B}^T) \right) dV + \frac{Pm}{E} \int_V \mathbf{B}_{20}^T \cdot \nabla^2 \mathbf{B}_{20}^T dV \end{aligned} \quad (9)$$

Since, Bullard's selection rule [10] (p 229) suggests  $\mathbf{u}^T$  and  $\mathbf{B}^T$  can not generate  $\mathbf{B}^P$ . Hence, the energy equation for  $\mathbf{B}_{10}^P$  becomes

$$\begin{aligned} \frac{Pm}{2E} \frac{d}{dt} \int_V |\mathbf{B}_{10}^P|^2 dV = \frac{Pm}{E} \int_V \mathbf{B}_{10}^P \cdot \left( \nabla \times (\mathbf{u}^P \times \mathbf{B}^P) + \nabla \times (\mathbf{u}^P \times \mathbf{B}^T) + \right. \\ \left. \nabla \times (\mathbf{u}^T \times \mathbf{B}^P) \right) dV + \frac{Pm}{E} \int_V \mathbf{B}_{10}^P \cdot \nabla^2 \mathbf{B}_{10}^P dV \end{aligned} \quad (10)$$

### 3. Results

The simulations has two steps. First, a pure hydrodynamic simulation is performed at each  $Ra$  number to obtain saturated state. Then, a seed magnetic field of  $\Lambda = 0.01$  is used in the saturated hydrodynamic state to start both kinematic and nonlinear dynamo simulations [6]. For kinematic simulations, Lorentz force term was dropped from mometum equation and start time-stepping all three equations [7]. For a frozen flow (saturated velocity field at a given time) we do not find any dynamo action in our low-E parameter regimes as classical kinematic theory deals with [9]. This suggests that Rossby wave plays an important role in magnetic field generation in the rapidly rotating spherical shell dynamo models [11]. The roles of drifting frequency of the columnar structure (for exmaple, Kumar-Roberts flow) on dynamo action is briefly studied in the framework of kinematic models [12]. The authors shown that for a given manetic magnetic Reynolds number ( $Rm$ ) the growth rate of dynamo increases with drifting frequency of the columns in wide range of the parameter space. Though in our study structure of the initial velocity field is far more complex. The focus of this study is to quantify the roles of rapid rotation and manetic field in polarity selection from a seed magnetic field ( $\Lambda = 0.01$ ) in the nonlinear and kinematic regimes. We perform calculations at two different Ekman numbers. To keep the effect of inertia

low on the simulations [13], we fix our parameters  $E = 1.2 \times 10^{-5}$ ,  $Pr = Pm = 5$  and  $E = 1.2 \times 10^{-6}$ ,  $Pr = Pm = 1$ . Table 1 summarises the details of simulations and computed value of Elsasser number at saturated nonlinear dynamos. For comparison purposes kinematic simulations are performed in each case.

### 3.1. Role of symmetry in polarity selection

Evolution of Elsasser numbers for different symmetries belong to dipole and quadrupole families for simulations at  $E = 1.2 \times 10^{-5}$ ,  $Pr = Pm = 5$ ,  $Ra = 140$  are shown in Fig. 1. For low- $Ra$  case, the symmetry of velocity field is preserved under rapid rotation i.e., the flow is symmetric about the equator. Such kind of flow preserve the equatorial symmetric or antisymmetric of the initial magnetic field throughout the simulations in a kinematic dynamo model. In this case we can see from Fig. 1 that the initial magnetic field belong to dipole family is growing while quadrupole symmetries are falling in both nonlinear and kinematic cases.

We choose to study further details about the role of symmetries of the velocity field and the magnetic field in polarity selection. To keep the analysis simple, we study the growth/fall of the axial dipole and axial quadrupole. Though, there is no dynamo action of pure axial dipole or axial quadrupole as Cowling's antidynamo theory suggests [14]. Nevertheless, we find that the growth of axial dipole is much higher than the any other field configuration in a successful dynamo. First, we consider an initial seed magnetic field ( $\Lambda = 0.01$ ) composed of 99.99% of  $\mathbf{B}_{20}^P$  and 0.01% of  $\mathbf{B}_{10}^P$  and continue the simulations in both kinematic and nonlinear models at  $Ra = 140$ . Fig. 2 (a) illustrates that successful dynamos in both nonlinear (red) and kinematic (blue) regimes unlike the case in Fig. 1 (c). Elsasser numbers of  $\mathbf{B}_{10}^P$  and  $\mathbf{B}_{20}^T$  for nonlinear dynamo cases in Fig. 2 (b) suggests that under preserved symmetry of velocity only axial dipole component of the field is growing and the axial quadrupole component is falling and saturated to a very small value due to back reaction effect. For kinematic case, we do expect the same behaviour, except the saturation and the axial quadrupole will continue to fall. In second case, we break the symmetry of velocity field by sowing equatorial antisymmetric component of 1% of total kinetic energy in case of initial



Table 1: Parameters used in kinematic and nonlinear dynamo simulations and computed  $E_m/E_k$ ,  $\Lambda$ ,  $\Lambda_{AD}$  for saturated nonlinear simulations.  $\Lambda_{AD}$  denotes Elsasser number based on magnetic energy contain in  $\mathbf{B}_{10}^P$  and  $\mathbf{B}_{20}^T$ . D corresponds to dipole and ND denotes nondipole magnetic field structure at the outer boundary of the spherical shell. For each  $Ra$ , a hydrodynamic simulation was performed to use the velocity field in the dynamo model.  $\mathbf{B}_{init}$  represents the starting magnetic field structure. For  $Ra = 140$ , symmetry of the velocity field is broken by sowing antisymmetric energy 1% of total kinetic energy.

$E$	$Ra$	$Pr = Pm$	$l_{max}$	$N_r$	$\mathbf{B}_{init}$	$\Lambda$	$\Lambda_{AD}$	$\mathbf{B}_{r=r_o}$
$1.2 \times 10^{-5}$	140	5	80	96	$\mathbf{B}_{10}^P$	0.11	0.09	D(D)
$1.2 \times 10^{-5}$	140	5	80	96	$\mathbf{B}_{20}^P$	no dynamo	—	—
$1.2 \times 10^{-5}$	140	5	80	96	$\mathbf{B}_{20}^P$ <sup>1</sup>	0.11	0.09 <sup>2</sup>	D(D)
$1.2 \times 10^{-5}$	140	5	80	96	$\mathbf{B}_{30}^P$	0.11	0.09	D(D)
$1.2 \times 10^{-5}$	140	5	80	96	$\mathbf{B}_{31}^P$	no dynamo	—	—
$1.2 \times 10^{-5}$	140	5	80	96	mixed <sup>3</sup>	0.11	0.09	D(D)
$1.2 \times 10^{-5}$	220	5	100	120	$\mathbf{B}_{10}^P$	0.99	0.37	D(ND)
$1.2 \times 10^{-5}$	220	5	100	120	$\mathbf{B}_{20}^P$	0.99	0.37 <sup>2</sup>	D(ND)
$1.2 \times 10^{-6}$	200	1	180	220	$\mathbf{B}_{10}^P$	0.1	0.08	D(D)
$1.2 \times 10^{-6}$	400	1	220	220	$\mathbf{B}_{10}^P$	0.98	0.35	D(ND)
$1.2 \times 10^{-6}$	400	1	220	220	$\mathbf{B}_{20}^P$	0.98	0.35 <sup>2</sup>	D(ND)
$3 \times 10^{-7}$	540	1	320	360	$\mathbf{B}_{20}^P$	1.56	0.35	D(ND)

<sup>1</sup> artificially break equatorial symmetry of the impose initial velocity field.

<sup>2</sup>  $\mathbf{B}_{20}^P$  convert to  $\mathbf{B}_{10}^P$ .

<sup>3</sup> 99.99%  $\Lambda_{20}^P$  + 0.01%  $\Lambda_{10}^P$ .

magnetic field of  $\mathbf{B}_{20}^P$  at same  $Ra$ . By doing so, we see that in Fig. 2 (c) that dynamo is growing and the harmonic analysis of energy of the nonlinear simulation in Fig. 2 (d) suggests that it is axial dipole component which is growing and axial quadrupole is falling. In high- $Ra$  case, where the symmetry of velocity field break down naturally under the rapid rotation, we see that in Fig. 2 (e and f) that starting with  $\mathbf{B}_{20}^P$  convert

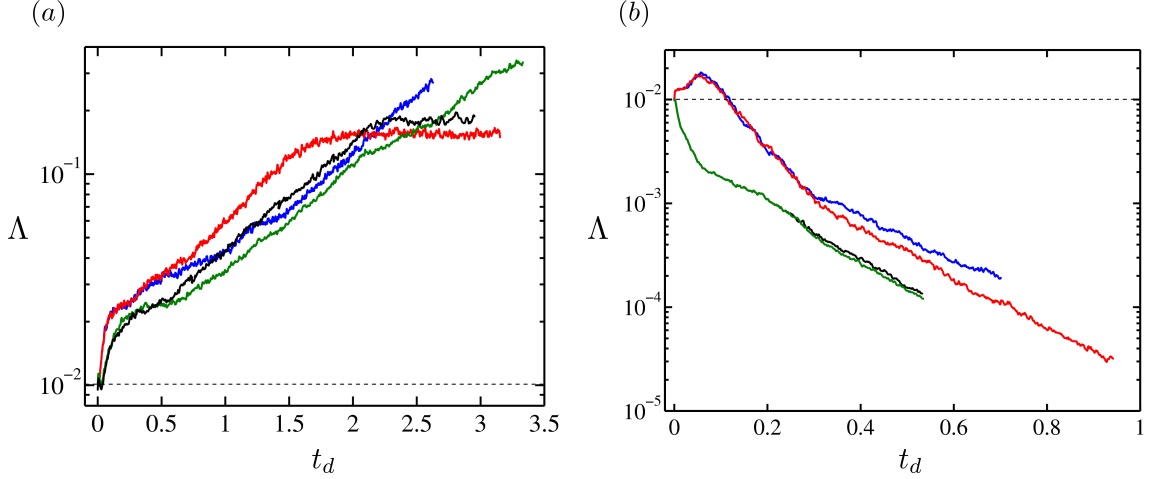


Figure 1: Evolution of Elsasser number with magnetic diffusion time for dynamo simulations at  $E = 1.2 \times 10^{-5}$ ,  $Pr = Pm = 5$ ,  $Ra = 140$ . The structure of starting seed magnetic field are - (a)  $\mathbf{B}_{10}^P$  (red and blue),  $\mathbf{B}_{30}^P$  (black and green) (b)  $\mathbf{B}_{30}^P$  (red and blue),  $\mathbf{B}_{31}^P$  (black and green). Red and black lines respresent nonlinear and black and green lines for kinematic cases.

itself into dipole. This happen due to the fact that nonlinear product of equatorial antisymmetric of  $\mathbf{u}$  and equatorial symmetric of  $\mathbf{B}$  give rise to an antisymmetric  $\mathbf{B}$  [15]. The initial axial quadrupole (equatorial symmetric structure) interacts with the antisymmetric components of the flow and induced equatorial antisymmetric magnetic field, belong to dipole family. This happen in the very early phase of the simulation and this flow-field interaction is purely a kinematic effect. Therefore, we get a growing dynamo.

We have tested the idea that for a rapidly rotating dynamo with equatorial symmetry broken flow always gives a successful dipolar dynamo by changing the initial structure of the magnetic field. In next paragraph, we explore the mechanisms to explain the failure of a quadrupolar dynamo and success of a dipolar dynamo.

For simplicity, we use dynamo models starting from axial dipole and axial quadrupole. To analysis the simulations, kinematic cases are used. Since, from Fig. 1(c – d) we do not see much differences between nonlinear and kinematic for quadrupole run, while for dipole case, we see a growing dipolar dynamo in both cases. Fig. 3 shows the axisym-

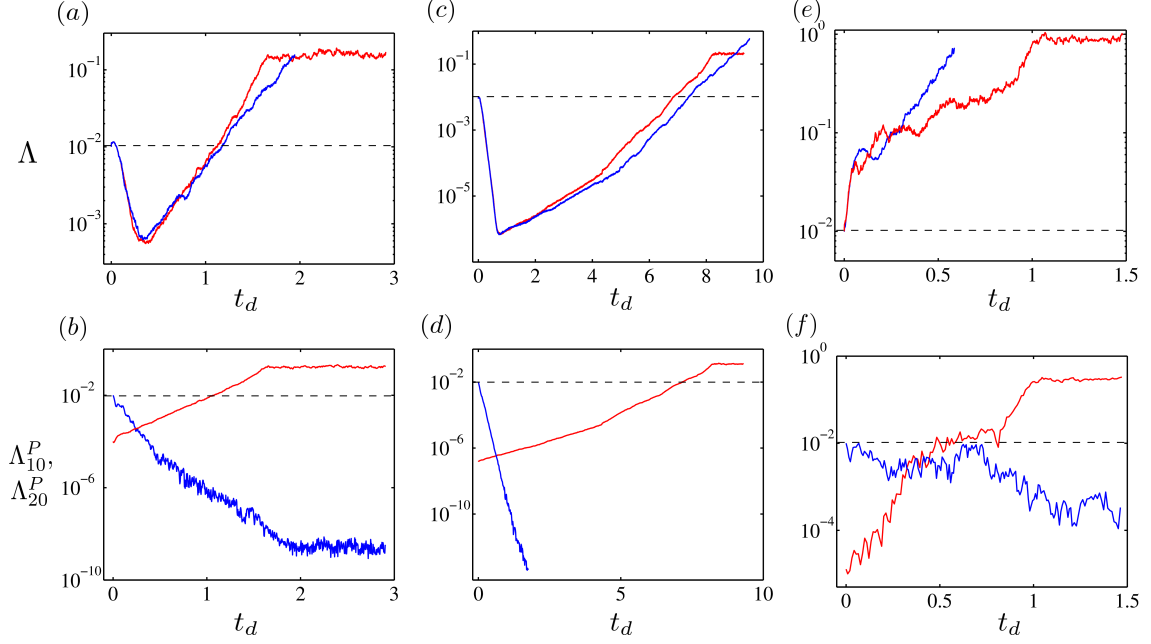


Figure 2: Evolution of Elsasser number of  $\mathbf{B}_{10}^P$  (red line) and  $\mathbf{B}_{20}^P$  (blue line) for the nonlinear dynamo simulations for  $E = 1.2 \times 10^{-5}$ ,  $Pr = Pm = 5$ . The structure of starting seed magnetic field are - (a) mixed (99.99%  $\Lambda_{20}^P + 0.01\%$   $\Lambda_{10}^P$ ) and (b) artificially broken velocity symmetry at  $Ra = 140$ . and (c)  $\mathbf{B}_{20}^P$  at  $Ra = 220$ .

metric  $B_\phi$  generation for dipole and quadrupole cases for kinematic dynamo simulations at  $Ra = 140$ . For dipole case, initially the axisymmetric toroidal field is generated by both shearing of axial magnetic field ( $B_z$ ) and radial magnetic field ( $B_s$ ) in cylindrical coordinate by differential rotation, known as  $\omega$ -effect [16]. Further in time, we see it is the shearing of  $B_z$  which supports the field generation. While in case of quadrupole, axisymmetric toroidal field is generated by a different mechanism from dipole and it is the radial magnetic field sheared by the zonal flow ( $u_\phi$ ) in cylindrical coordinate. Time evolutions of Elsasser number for quadrupole case (Fig. 1 (c)), suggests that there is an initial peak for short period of time and then it is falling in time. This peak is attribute to the initial  $B_\phi$  generation. As we go for more complex field structure (for example,  $\mathbf{B}_{31}^P$ ), we do not see any peak in magnetic energy and from beginning of the simulation, the dynamo is falling. For axial dipole case,  $B_s$  is well above the equatorial plane. This suggests that the columnar structure of the flow helps to re-

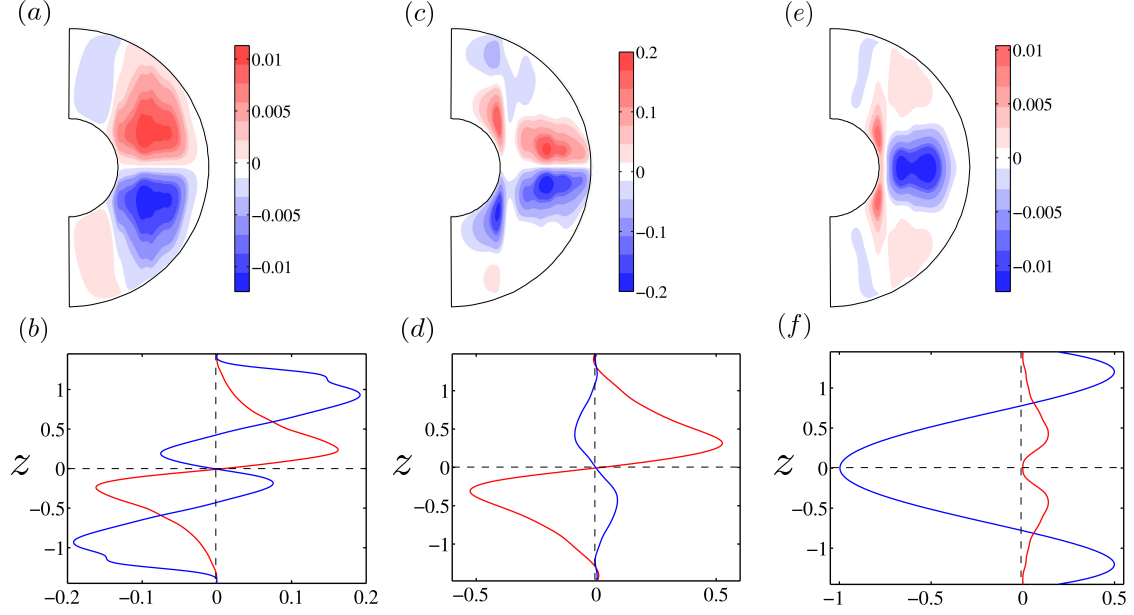


Figure 3: Snapshots of axisymmetric  $B_\phi$  generation for kinematic dynamo simulations at  $E = 1.2 \times 10^{-5}$ ,  $Pr = Pm = 5$ ,  $Ra = 140$ . The snapshots of first and third columns are at  $t_d = 3 \times 10^{-2}$  and the second column at  $t_d = 1.5$ . Upper column shows snapshots of  $B_\phi$  and bottom shows the generation terms. Red and blue lines represent  $s - \phi$  averaged of  $B_z \partial u_\phi / \partial z$  and  $B_s \partial u_\phi / \partial s$  respectively.

generate poloidal field from a toroidal field through a classical  $\alpha$ -effect [16] at least in the kinematic regime and became a successful dynamo. Though, there is a difference in axial dipole field generation between nonlinear and kinematic dynamo models. We will pursue this issue in coming subsection. As in case of quadrupole, maximum value of  $B_\phi$  is confined to the equator plane. Hence, the flow failed to generate any further poloidal magnetic field from the toroidal field through Parker classical  $\alpha$ -effect [16]. Therefore, the dynamo regeneration cycle (Toroidal  $\leftrightarrow$  Poloidal) is stopped and become a failed dynamo. Nevertheless, it is clear the initial magnetic field structure determines fate of the dynamos in both kinematic and nonlinear case as long as rapid rotation maintains symmetry of the velocity field.

### 3.2. Role of back reaction in polarity selection

In this study, we focus on generation of the dipole field. Therefore, for simplicity we wish to restrict on the  $Y_1^0$  of poloidal and  $Y_2^0$  of toroidal magnetic field. We separate these two harmonics from the induction equation and study their growth with time.

Fig. 4 shows the generation of  $\mathbf{B}_{20}^T$  in nonlinear dynamo simulation for case of  $E = 1.2 \times 10^{-5}$ ,  $Pr = Pm = 5$ ,  $Ra = 220$  starting magnetic field as  $\mathbf{B}_{10}^P$ . Though as we see in the previous section that the starting magnetic structure does not play any role in the case of high- $Ra$ . Fig. 4 (a) shows the energy contribution to  $\mathbf{B}_{20}^T$  through Eq. 9. The energy supplied to  $\mathbf{B}_{20}^T$  is calculated using

$$\Gamma_{20}^T = \int_V \mathbf{B}_{20}^T \cdot \nabla \times (\mathbf{u} \times \mathbf{B}) dV \quad (11)$$

and apply Bullard selection rule for different combinations of  $\mathbf{u}$  and  $\mathbf{B}$ . The maximum contribution is coming from induction term consists of  $\mathbf{u}^T$  and  $\mathbf{B}^P$  (red line) and majorly it is axisymmetric structures (green line) that is contributing in the generation. Interestingly, there is no major role of back reaction of the magnetic field in changing the mechanism of generation, except saturation of the field. This suggests that the classical- $\omega$  effect is valid in nonlinear regime too as demonstrated previous [17]. As classical- $\omega$  effect suggests that it is the large scale flow that supports the azimuthal field. To verify this idea, we construct a energy matrix based on Bullard's selection rule [10] by keeping the structure of flow ( $\mathbf{u}^T$ ) and field ( $\mathbf{B}^P$ ) as axisymmetric ( $m = 0$ ). The bottom panel of Fig 4 shows the energy contribution of different degrees of the flow and field to the  $\mathbf{B}_{20}^T$  at two different snapshot times ( $t_d = 0.414$  and  $t_d = 0.522$ ). Since our model start with a seed magnetic field, so we do expect the effect of back reaction on the flow after some time. For Fig. (b), the energy matrix suggests that it is  $Y_1^0$  of the toroidal flow that is helping in  $\mathbf{B}_{20}^T$  generation. While for Fig. (c), it is  $Y_1^0$  component of the toroidal flow supports the field. This clearly shows effect of back reaction on the large scale flow in time. This effect is attribute to effect of toroidal magnetic force on large scale zonal flow. In Fig. 5 shows the structure of time and azimuthally averaged zonal flow for non-magnetic (a) and nonlinear dynamo

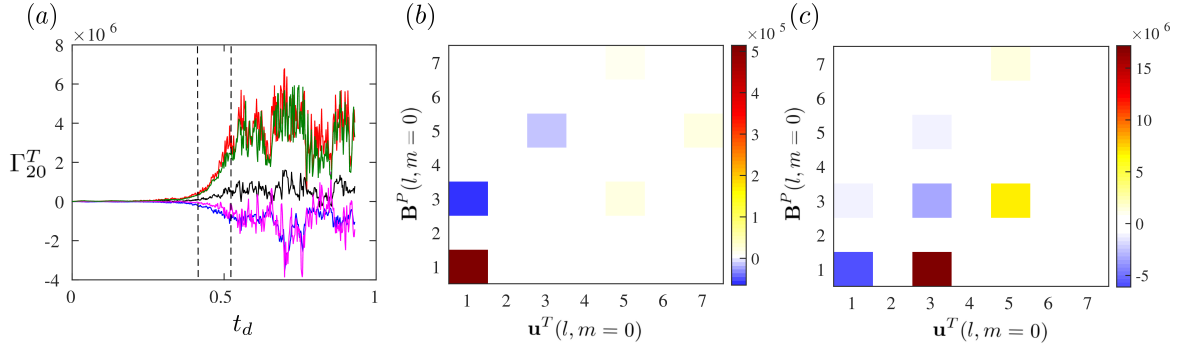


Figure 4:  $\mathbf{B}_{20}^T$  generation mechanism in terms of energy for  $E = 1.2 \times 10^{-5}$ ,  $Ra = 220$ . The top panel represents volume averaged of induction term dotted with  $\mathbf{B}_{20}^T$ . The lines represent - red -  $(Pm/E)\mathbf{B}_{20}^T \cdot \nabla \times (\mathbf{u}^T \times \mathbf{B}^P)$ , blue -  $(Pm/E)\mathbf{B}_{20}^T \cdot \nabla \times (\mathbf{u}^P \times \mathbf{B}^T)$ , black -  $(Pm/E)\mathbf{B}_{20}^T \cdot \nabla \times (\mathbf{u}^P \times \mathbf{B}^P)$ , magenta -  $(Pm/E)\mathbf{B}_{20}^T \cdot \nabla \times (\mathbf{u}^T \times \mathbf{B}^T)$  and green -  $(Pm/E)\mathbf{B}_{20}^T \cdot \nabla \times (\mathbf{u}_{10}^T \times \mathbf{B}_{10}^T)$ . The bottom panel represents energy matrix for  $(Pm/E)\mathbf{B}_{20}^T \cdot \nabla \times (\mathbf{u}^T(m=0) \times \mathbf{B}^P(m=0))$  at two different times. (b) is at  $t_d = 0.414$  and (c) is at  $t_d = 0.522$ .

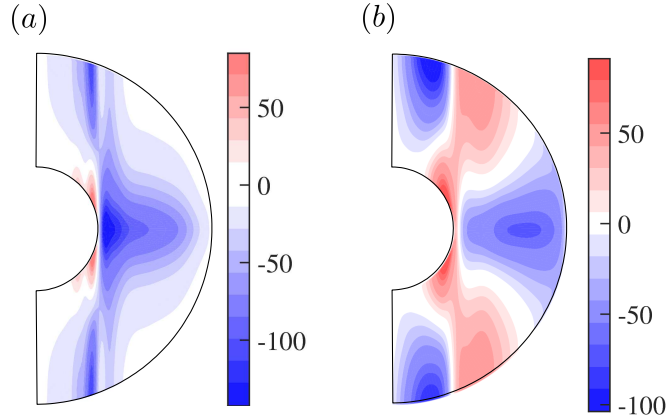


Figure 5: Meridional plots of time and azimuthally averaged zonal flow for simulations at  $E = 1.2 \times 10^{-5}$ ,  $Ra = 220$ . (a) represents non-magnetic and (b) nonlinear dynamo in saturated phase.

(b) models in the saturated state. For non-magnetic case, structure of the zonal flow is geostrophic (dominantly  $Y_1^0$ ), where as for nonlinear case, the dominant structure is mostly dominated by  $Y_3^0$  [18]. Therefore, we see a close analogy between energy matrices and zonal flow structures.

As we see in the previous paragraph that, axial dipole plays a major role in  $\mathbf{B}_{20}^T$

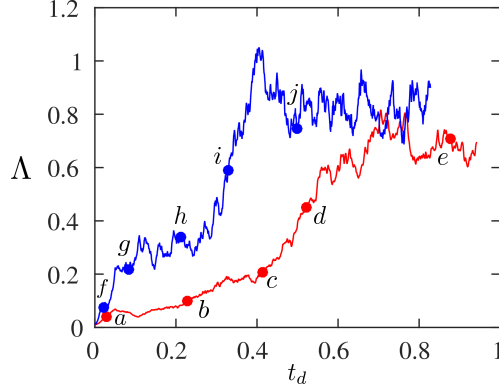


Figure 6: Evolution of Elsasser number for nonlinear dynamo simulations at  $E = 1.2 \times 10^{-5}$ ,  $Pr = Pm = 5$   $Ra = 220$  (red) and  $E = 1.2 \times 10^{-6}$ ,  $Pr = Pm = 1$   $Ra = 400$  (blue). The alphabet numberings correspond to the snapshot times of Fig. 7.

generation. Now, we look into mechanism of  $\mathbf{B}_{10}^P$  generation. Here also case of starting magnetic field as axial dipole is considered. However we find that at low- $Ra$  regime, (for example, case at  $E = 1.2 \times 10^{-5}$ ,  $Ra = 140$ ) the poloidal magnetic field is dipolar structure in both kinematic and nonlinear dynamo models. However, differences in magnetic field structure between kinematic and nonlinear dynamos show up at high- $Ra$  ( $Ra = 220$ ). We look at snapshots of radial magnetic field at outer boundary of the spherical shell of different time instants of the nonlinear simulations. Fig. 6 shows total Elsasser number of dynamo models at two different  $E$ . Fig. 7 shows snapshots of radial magnetic field at outer boundary for nonlinear dynamo simulations. Very beginning of the simulations both show a dipolar structure at the outer boundary. As time progress both dynamos show a multipolar structure. We further integrate our simulations to see if any difference arises. We observe an interesting and quite distinct behavior in the nonlinear simulations. After some time the magnetic field switch back to dipolar structure at the outer boundary of spherical shell and it happens much earlier than the saturation stage. Though one would not expect this kind of behaviour in kinematic models. The magnetic field shows a first dipolar structure at  $t_d = 0.522$  and  $t_d = 0.329$  at  $E = 1.2 \times 10^{-5}$  and  $E = 1.2 \times 10^{-6}$ , respectively (see, Fig. 6, point

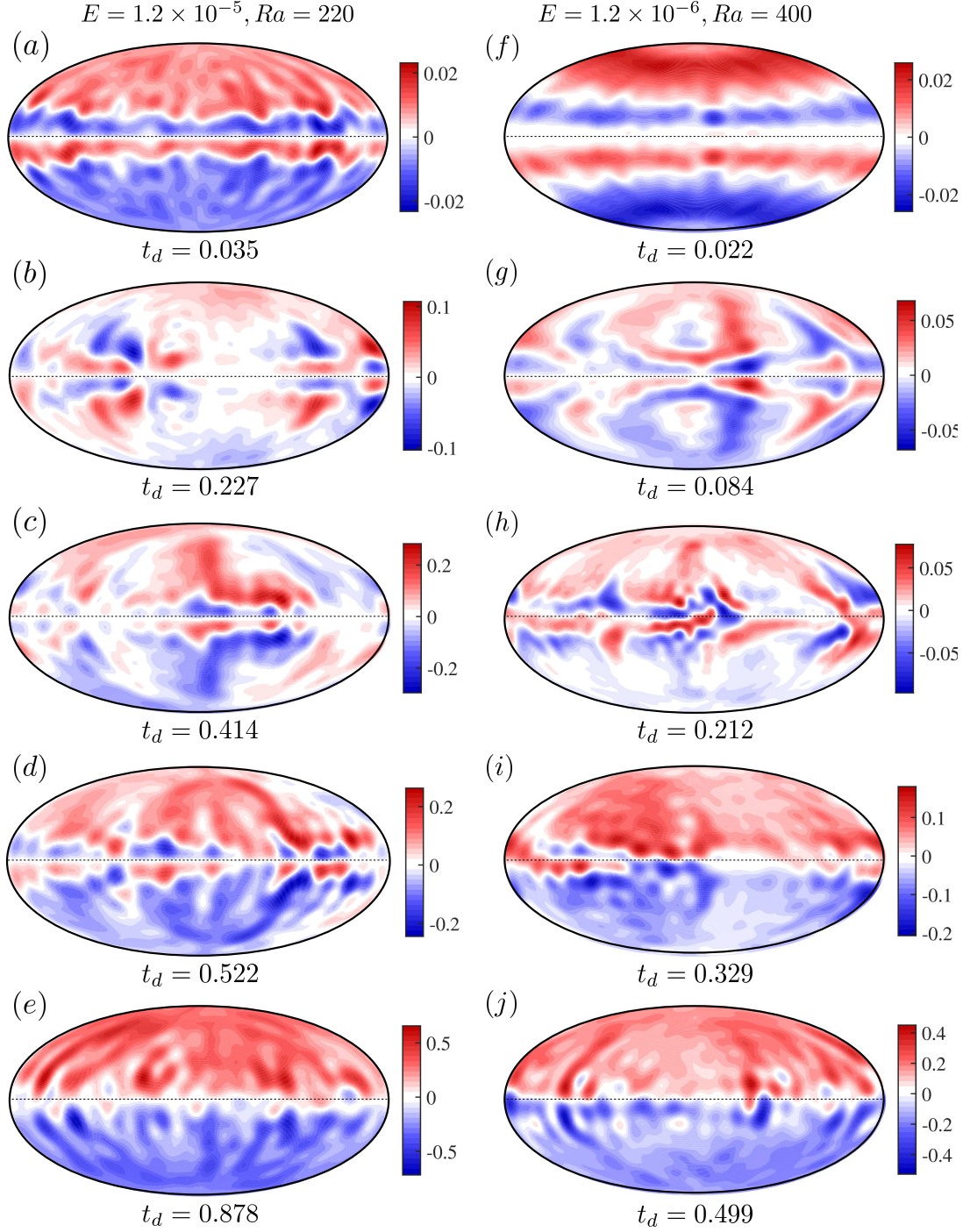


Figure 7: Evolution of radial magnetic field at the outer boundary for nonlinear dynamo simulations. The model parameters are given at top of the figure. Snapshot times are given below of each figure.

‘ $d$ ’ and ‘ $i$ ’). The corresponding total Elsasser numbers are 0.42 and 0.59, which is well before saturation of the rapidly rotating nonlinear dynamos. Therefore, this unique behavior of the nonlinear dynamo is solely due to the back reaction of the magnetic



field. This event can be better visualise in a video. This behavior suggests that back reaction able to modify structure of the flow (therefore, helicity associates with the columnar flows) and bring back the dipolar structure well before saturation of the dynamo. This study suggests that the magnetic field can effect the flow much earlier than the saturation, even though Elsasser number is not high enough.

Fig. 8 shows evolution of Elsasser number based on axial dipole ( $\Lambda_{10}^P$ ) and generation of axial dipole at two different  $E$ . Note that te initial Elsasser number is very small ( $\Lambda_{10}^P = 0.01$ ). The motivation is to trace the effect of the back reaction through the axial dipole generaion. The middle panel of Fig. 8 shows the contribution to the magneic energy of  $B_{10}^P$  by flow-field interaction in the induction equation. Indcution term is separated into four combinatons of toroidal-poloidal decompositions of flow and field. Out of these four we see only two of them ( $\nabla \times (\mathbf{u}^T \times \mathbf{B}^P)$  and  $\nabla \times (\mathbf{u}^P \times \mathbf{B}^T)$ ) are contributing in the generation. The red line represents energy coming from  $\nabla \times (\mathbf{u}^T \times \mathbf{B}^P)$  and blue line shows energy coming from  $\nabla \times (\mathbf{u}^P \times \mathbf{B}^T)$ . The two plots show that initially blue line is positive and red is negative and after a while they changed signed. This bifurcation point indicates when effect of back reaction becomes important in each dynamo simualation. Hence, we see a clear transition between kinematic and nonlinear phase in a self-consistent nonlinear dynamo model. Though before the bifuraction (kinematic phase) the values are too small to see them in magnitude wise. To see which term dominates in this phase, we substract blue line from red line and the difference is defined as  $G_{10}^P$ .

$$G_{10}^P = \int_V \left( \mathbf{B}_{10}^P \cdot \nabla \times (\mathbf{u}^T \times \mathbf{B}^P) - \mathbf{B}_{10}^P \cdot \nabla \times (\mathbf{u}^P \times \mathbf{B}^T) \right) dV \quad (12)$$

The bottom panel of Fig. 8 shows zoomed of the  $G_{10}^P$  for the two dynamo models. It suggests that initially  $G_{10}^P$  is negative and then becomes positive. This ngetaive value shows the dominance of  $\nabla \times (\mathbf{u}^P \times \mathbf{B}^T)$  in the kinematic phase. This refers to a transitional behaviour in the solution in the presence of the Lorentz force. By visualization we can see the difference of higher magnitude of red line than blue line after the bifurcation till saturation of the dynamo. This confirms a positive growth

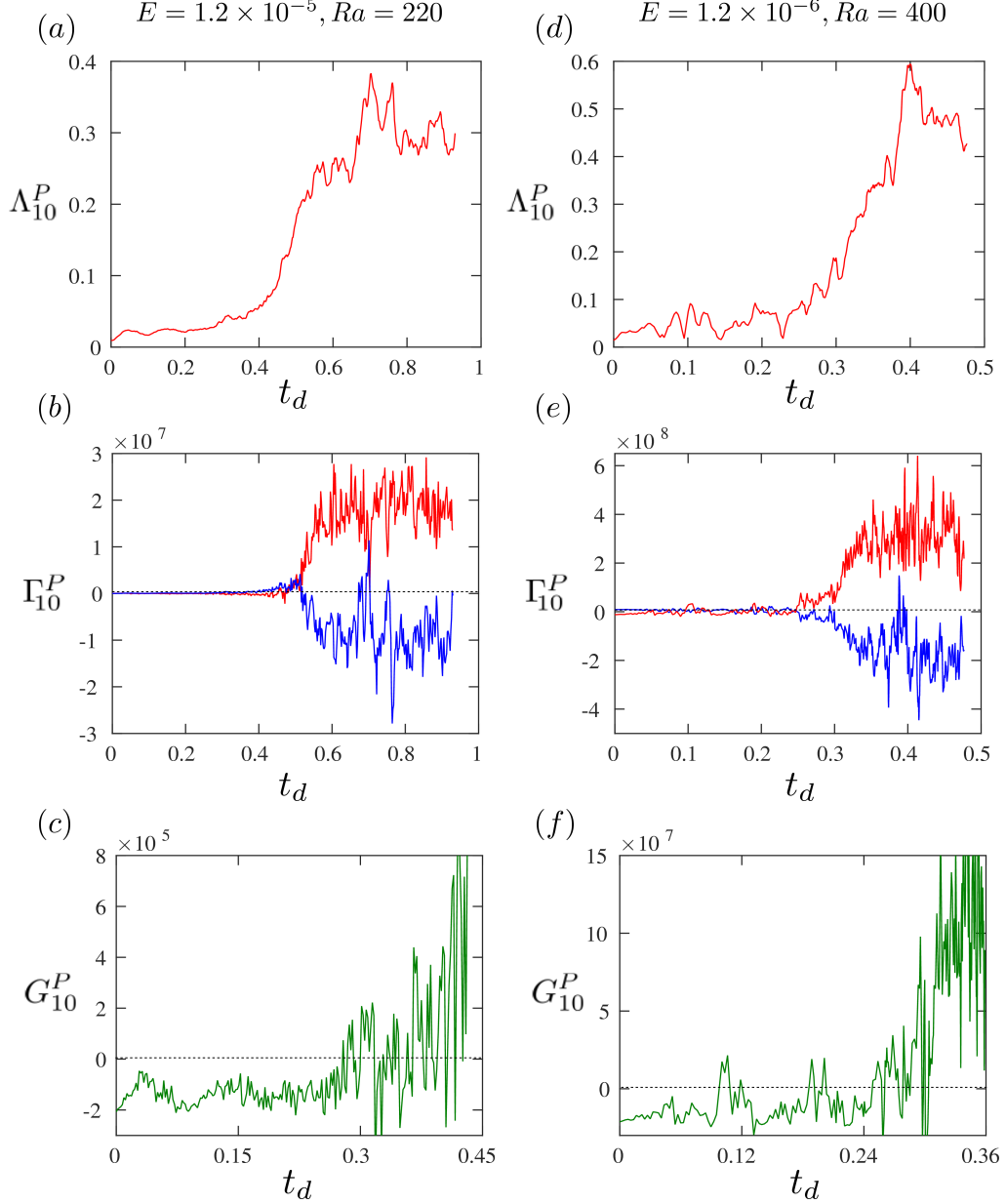


Figure 8: (a) and (d) show evolution of Elsasser number of  $\mathbf{B}_{10}^P$  for dynamo simulations at two different  $E$ . (b) and (e) show energy contribution to  $\mathbf{B}_{10}^P$ . Red line represent  $(Pm/E)\mathbf{B}_{10}^P \cdot \nabla \times (\mathbf{u}^T \times \mathbf{B}^P)$ ; Blue line represent  $(Pm/E)\mathbf{B}_{10}^P \cdot \nabla \times (\mathbf{u}^P \times \mathbf{B}^T)$ . (c) and (f) show difference of red and blue lines.

of the axial dipole after the bifurcation. In the saturation state, the net positive value will balance by negative value of the dissipation of the axial dipole.

The dynamo model consists of full spectrum of the flow and magnetic field. Therefore, it is difficult to visualize how small scale flows and fields are interacting with each

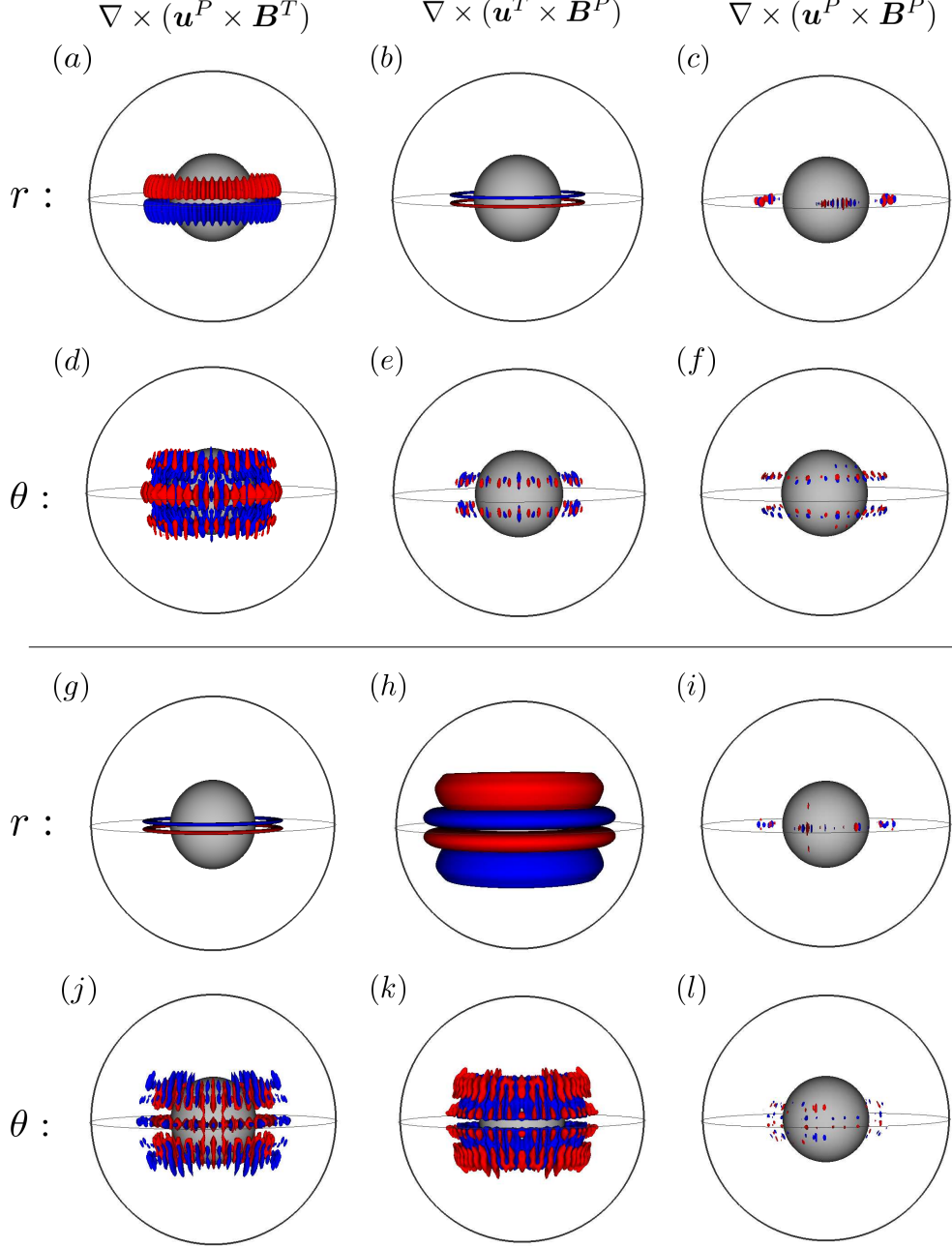


Figure 9: Isosurfaces of  $r$  and  $\theta$  components of induction terms for nonlinear simulation at  $E = 1.2 \times 10^{-6}$ ,  $Pr = Pm = 1$ ,  $Ra = 400$ . Two snapshots are separated by horizontal line. The top ( $a - f$ ) is at  $t_d = 0.2$  and bottom ( $g - l$ ) is at  $t_d = 0.38$ . The contour levels for ( $a - f$ ) are  $\pm 5$  and ( $g - l$ ) are  $\pm 20$ .

others and producing a large scale magnetic field (herein, axial dipole) as suggested by mean field theory [19]. In this case, Bullard's selection works quite good way to help in finding the scale of flow and field and to see their interaction. The initial

stage of the nonlinear simulation behaves as kinematic. Therefore, we compare two snapshot times, one in early phase and another is further in time (before saturation of the dynamo) of the simulation to see the differences in mechanisms to generate the axial dipole in the simulation. For that, we choose two snapshots at  $t_d = 0.2$  (kinematic phase) and  $t_d = 0.55$  (nonlinear phase). Fig. 9 shows isosurface snapshots of  $\nabla \times (\mathbf{u}^P \times \mathbf{B}^T)$ ,  $\nabla \times (\mathbf{u}^T \times \mathbf{B}^P)$  and  $\nabla \times (\mathbf{u}^P \times \mathbf{B}^P)$  for nonlinear simulation at  $E = 1.2 \times 10^{-6}$ ,  $Ra = 400$  at two different snapshot times ( $t_d = 0.2$  and  $0.38$ ) separated by a horizontal line. The values of  $l$  and  $m$  are truncated at 30 while using Bullard's selection rule. Below  $l$  and  $m = 30$ , there is no significant differences in structures. Fig. 9 ( $a, b$  and  $e, f$ ) show the  $r$  components and ( $c, d$  and  $g, h$ ) show the  $\theta$  components of the decompositions. Comparison across  $r$  and  $\theta$  components of induction terms above the horizontal line suggests that it is induction term  $\nabla \times (\mathbf{u}^P \times \mathbf{B}^T)$  that is contributing to the axial dipole generation. The interaction of small scale flow and field is clearly evident in the dominant induction term. For  $r$  component it is antisymmetric and for  $\theta$  component it is symmetric, though there is a sign change from negative to positive across radial direction which also present in the  $\theta$  component of the axial dipole. Figures below the line show it is  $\nabla \times (\mathbf{u}^T \times \mathbf{B}^P)$  that is positively contributing to the both  $r$  and  $\theta$  components of the axial dipole. Though in the  $\theta$  component it is  $\nabla \times (\mathbf{u}^T \times \mathbf{B}^P)$  which is positively correlate with axial dipole while  $\nabla \times (\mathbf{u}^P \times \mathbf{B}^T)$  is negatively correlate. Therefore in the energy analysis, we see a positive contribution from  $\nabla \times (\mathbf{u}^T \times \mathbf{B}^P)$  and negative from  $\nabla \times (\mathbf{u}^P \times \mathbf{B}^T)$  as time progress. However the  $r$  component of  $\nabla \times (\mathbf{u}^T \times \mathbf{B}^P)$  shows a large scale axisymmetric structure and having a sign of change across each hemisphere. Since we use Bullard's selection to rule to calculate the terms for axial dipole, so there is a overlap of range of  $l$  which contribute to other harmonics of magnetic fields (for example, octupole). Though in both snapshot times  $\nabla \times (\mathbf{u}^P \times \mathbf{B}^P)$  is negligible.

Now we look into components of the induction term through axial dipole is getting generated. So for this we expand the induction in terms of stretching and advection.

The expanded form of  $\nabla \times (\mathbf{u}^P \times \mathbf{B}^T)$  is

$$\begin{aligned} \nabla \times (\mathbf{u}^P \times \mathbf{B}^T) = & \underbrace{\left[ \frac{B_\theta}{r} \frac{\partial u_r}{\partial \theta} \right]}_I + \underbrace{\left[ \frac{B_\phi}{r \sin \theta} \frac{\partial u_r}{\partial \phi} \right]}_{II} \hat{\mathbf{e}}_r \\ & + \underbrace{\left[ \frac{B_\theta}{r} \frac{\partial u_\theta}{\partial \theta} \right]}_{III} + \underbrace{\left[ \frac{B_\phi}{r \sin \theta} \frac{\partial u_\theta}{\partial \phi} \right]}_{IV} + \left[ \frac{B_\theta u_r}{r} \right] \hat{\mathbf{e}}_\theta \\ & - \left[ u_r \frac{\partial B_\theta}{\partial r} + \frac{u_\theta}{r} \frac{\partial B_\theta}{\partial \theta} + \frac{u_\phi}{r \sin \theta} \frac{\partial B_\theta}{\partial \phi} \right] \hat{\mathbf{e}}_\theta \end{aligned} \quad (13)$$

Similarly,  $\nabla \times (\mathbf{u}^T \times \mathbf{B}^P)$  is expand as

$$\begin{aligned} \nabla \times (\mathbf{u}^T \times \mathbf{B}^P) = & - \underbrace{\left[ \frac{u_\theta}{r} \frac{\partial B_r}{\partial \theta} \right]}_V + \underbrace{\left[ \frac{u_\phi}{r \sin \theta} \frac{\partial B_r}{\partial \phi} \right]}_{VI} \hat{\mathbf{e}}_r \\ & + \underbrace{\left[ B_r \frac{\partial u_\theta}{\partial r} \right]}_{VII} + \underbrace{\left[ \frac{B_\theta}{r} \frac{\partial u_\theta}{\partial \theta} \right]}_{VIII} + \left[ \frac{B_\phi}{r \sin \theta} \frac{\partial u_\theta}{\partial \phi} \right] \hat{\mathbf{e}}_\theta \\ & - \left[ \frac{u_\theta}{r} \frac{\partial B_\theta}{\partial \theta} + \frac{u_\phi}{r \sin \theta} \frac{\partial B_\theta}{\partial \phi} + \frac{u_\theta B_r}{r} \right] \hat{\mathbf{e}}_\theta \end{aligned} \quad (14)$$

Table 2 and Table 3 show the volume averaged of over top hemisphere of induction terms ( $\nabla \times (\mathbf{u}^P \times \mathbf{B}^T)$  and  $\nabla \times (\mathbf{u}^T \times \mathbf{B}^P)$ ) and its decomposition as shown in Eq. 13 and Eq. 14 for two different time instants at  $t_d = 0.2$  and  $0.35$ . Fig. 10 shows the dominant terms of decompositions of  $\nabla \times (\mathbf{u}^P \times \mathbf{B}^T)$  as defined in Eq. 13. The terms are calculated by Bullard selection rule. The snapshots are shown at  $t_d = 0.2$ . The  $r$  and  $\theta$  components of axial dipole are getting generated from deformation of the small scale  $B_\phi$  by  $u_r$  and  $u_\theta$ , respectively. This suggests that for primary flow (rotation of the columns about its vertical axis) is responsible for  $B_r$  and the seconadry flow (up and down flow inside the column) is responsible for the generation of  $B_\theta$  of the axial dipole [8]. This argument is based on low- $Rm$  approximation, where first order smoothing approximation is relevant. [20]. Here length scale of  $Rm$  is based on thickness of the roll. Nevertheless, we find that till  $t_d = 0.3$  the growth of axial dipole is very weak for  $E = 1.2 \times 10^{-6}$ ,  $Ra = 400$  (see, Fig. 8 (b)). The dominant structures of the stretching terms are similar to the dominant induction term as shown in Fig. 9. For radial

field we can see the antisymmetric structure above and below of the equator plane, mimicing  $Y_1^0$  strcuture of the poloidal field while for  $\theta$  component it is symmetric about the equator. In both case the interaction between small scale structures flows and fields are notable.

Table 2: Volume averaged over top hemisphere of r-component of induction term and its decomposition as shown in Eq. 13 and Eq. 14. The values reported are here at two different time instants ( $t_d = 0.2$  and  $0.38$ ).

$t_d$	0.2	0.38	$t_d$	0.2	0.38
$\nabla \times (\mathbf{u}^P \times \mathbf{B}^T)_r$	10.36	-0.98	$\nabla \times (\mathbf{u}^T \times \mathbf{B}^P)_r$	1.36	24.98
$(B_\theta/r)(\partial u_r/\partial\theta)$	8.36	-0.54	$-(u_\theta/r)(\partial B_r/\partial\theta)$	0.56	23.74
$(B_\phi/r\sin\theta)(\partial u_r/\partial\phi)$	2.05	-0.44	$-(u_\phi/r\sin\theta)(\partial B_r/\partial\phi)$	0.75	0.54

Table 3: Volume averaged over top hemisphere of  $\theta$ -component of induction term and its decomposition as shown in Eq. 13 and Eq. 14. The values reported are here at two different time instants ( $t_d = 0.2$  and  $0.38$ )

$t_d$	0.2	0.38	$t_d$	0.2	0.38
$\nabla \times (\mathbf{u}^P \times \mathbf{B}^T)_\theta$	-12.36	20.54	$\nabla \times (\mathbf{u}^T \times \mathbf{B}^P)_\theta$	0.22	-30.54
$(B_\theta/r)(\partial u_\theta/\partial\theta)$	-2.42	18.54	$B_r(\partial u_r/\partial\theta)$	0.12	-24.62
$(B_\phi/r\sin\theta)(\partial u_\theta/\partial\phi)$	-10.36	0.53	$(B_\theta/r)(\partial u_\theta/\partial\theta)$	0.16	-2.94
$-u_r(\partial B_\theta/\partial r)$	0.36	0.42	$(B_\phi/r\sin\theta)(\partial u_\theta/\partial\phi)$	0.21	-1.57
$-(u_\theta/r)(\partial B_\theta/\partial\theta)$	0.22	0.18	$-(u_\theta/r)(\partial B_\theta/\partial\theta)$	0.13	0.94
$-(u_\phi/r)(\partial B_\theta/\partial\phi)$	0.18	0.22	$-(u_\phi/r)(\partial B_\theta/\partial\phi)$	0.17	0.83

Though the above mechanism is not valid as the magnetic field effects the flow. Fig. 11 shows the dominant terms of decompositions of  $\nabla \times (\mathbf{u}^T \times \mathbf{B}^P)$  as defined in Eq. 14. The terms are calculated by Bullard selection rule. The snapshots are shown at  $t_d = 0.38$ . Fig. (a, b) and (c, d) show  $r$  and  $\theta$  component of the induction

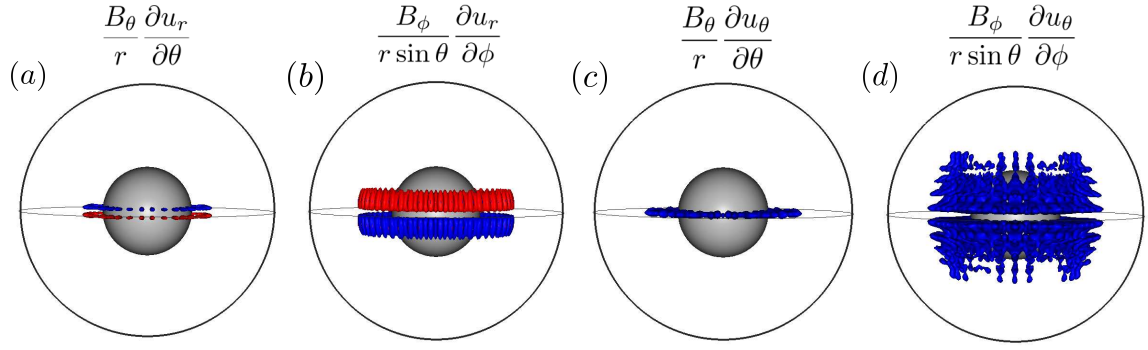


Figure 10: Isosurfaces of decompositions of  $\nabla \times (\mathbf{u}^P \times \mathbf{B}^T)$  for nonlinear simulation at  $E = 1.2 \times 10^{-6}$ ,  $Pr = Pm = 1$ ,  $Ra = 400$ . The snapshot time is at  $t_d = 0.2$ . The contour levels is  $\pm 5$ .

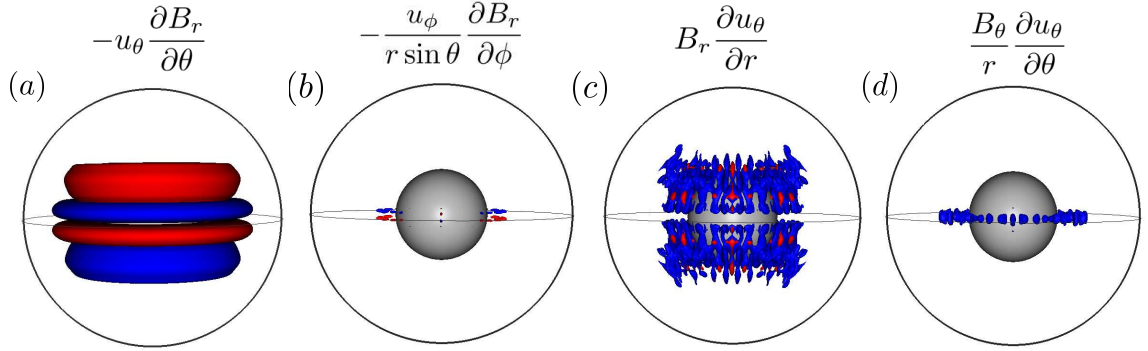


Figure 11: Isosurfaces of decompositions of  $\nabla \times (\mathbf{u}^T \times \mathbf{B}^P)$  for nonlinear simulation at  $E = 1.2 \times 10^{-6}$ ,  $Pr = Pm = 1$ ,  $Ra = 400$ . The snapshot time is at  $t_d = 0.38$ . The contour levels is  $\pm 20$ .

term. The dominant contributions for  $r$  and  $\theta$  components of the axial dipole is coming from  $-(u_\theta/r)\partial B_r/\partial\theta$  and  $B_r\partial u_\theta/\partial r$ . Note that the dominant structures of the terms are similar to the induction terms as shown in Fig. 9 The  $r$  component is supported by a advection of the radial field. Though, advection does not contribute in overall magnetic energy. The term analysis of  $\nabla \times (\mathbf{u}^T \times \mathbf{B}^P)$  (refer to Eq. 14) suggests that there is no stretching term to contribute to the radial component of axial dipole. Hence, this is a unique behaviour of nonlinear simulations. Though we have not looked into the transport coefficients of mean field theory using test field method as done by many authors in rotating spherical shell dynamos [21] [22] [23]. The advection of

mean magnetic flux by a mean flow is denoted by  $\gamma$  (see Eq. 11 of [23]). Schrunner et. al [23] showed that out of three combination of  $\gamma$ ,  $\gamma_\theta$  is contributing more in the generation of mean field.  $\gamma_\theta$  represents advection of the mean field in  $\theta$  direction. The coefficients of mean field suggests that the advection played an important role in preference of dipole in the context of rotating nonlinear dynamos [23]. Nevertheless, this structure of advection is similar to the advection of the mean field in meridional direction ( $\gamma_\theta$ ) as shown by Schrunner et. al [17]. Fig. 10 shows the energy contribution to  $\theta$  component of the axial dipole. It shows that the dominant contribution is coming from the stretching term  $B_r \partial u_\theta / \partial r$ . The  $\theta$  component of the axial dipole is contributed by  $B_r \partial u_\theta / \partial r$ . Note that this term is zero at equator because  $B_r$  is zero. Though meridional component of axial dipole is not zero and therefore, we see a non negligible contribution from  $(B_\theta / r) \partial u_\theta / \partial r$ .

### 3.2.1. Effect of Lorentz force in energy transfer

Next, we look into effect of the magnetic field on the flow. One of the way to quantify to look into energy spectra in the saturated phase and compare between nonmagnetic and nonlinear dynamo models. To see effect of the magnetic field, time averaged of  $u_z$  and  $u_s$  is calculated in both saturated phase of non-magnetic and nonlinear models. Fig. 12 (a and c) shows time averaged of  $u_z$  and  $u_s$  at two different  $E$ . The dotted and solid lines (red -  $u_z$  and blue -  $u_s$ ) shows saturated non-magnetic and nonlinear models, respectively. Fig. (b and d) shows difference of kinetic energy between nonlinear and non-magnetic models as defined as  $\Delta E$ . Comparison between nonlinear dynamo and non-magnetic energy spectra suggests that the Lorentz force acts different way in different scales. Enhancement of  $u_z$  and  $u_s$  (for example,  $l \leq 30$  at  $E = 1.2 \times 10^{-6}$ ) in case of nonlinear dynamo over non-magnetic case suggest that the Lorentz force acts to relax the geostrophic constraint imposed by the rotation, preferring a scale of convection larger than in absence of the magnetic field [24]. Though, in the small scale, transfer of the kinetic to magnetic energy through Lorentz force causes a lower kinetic energy than non-magnetic. Traditional idea is that the effect of Lorentz force is only visible when the nonlinear dynamo model saturates. However,



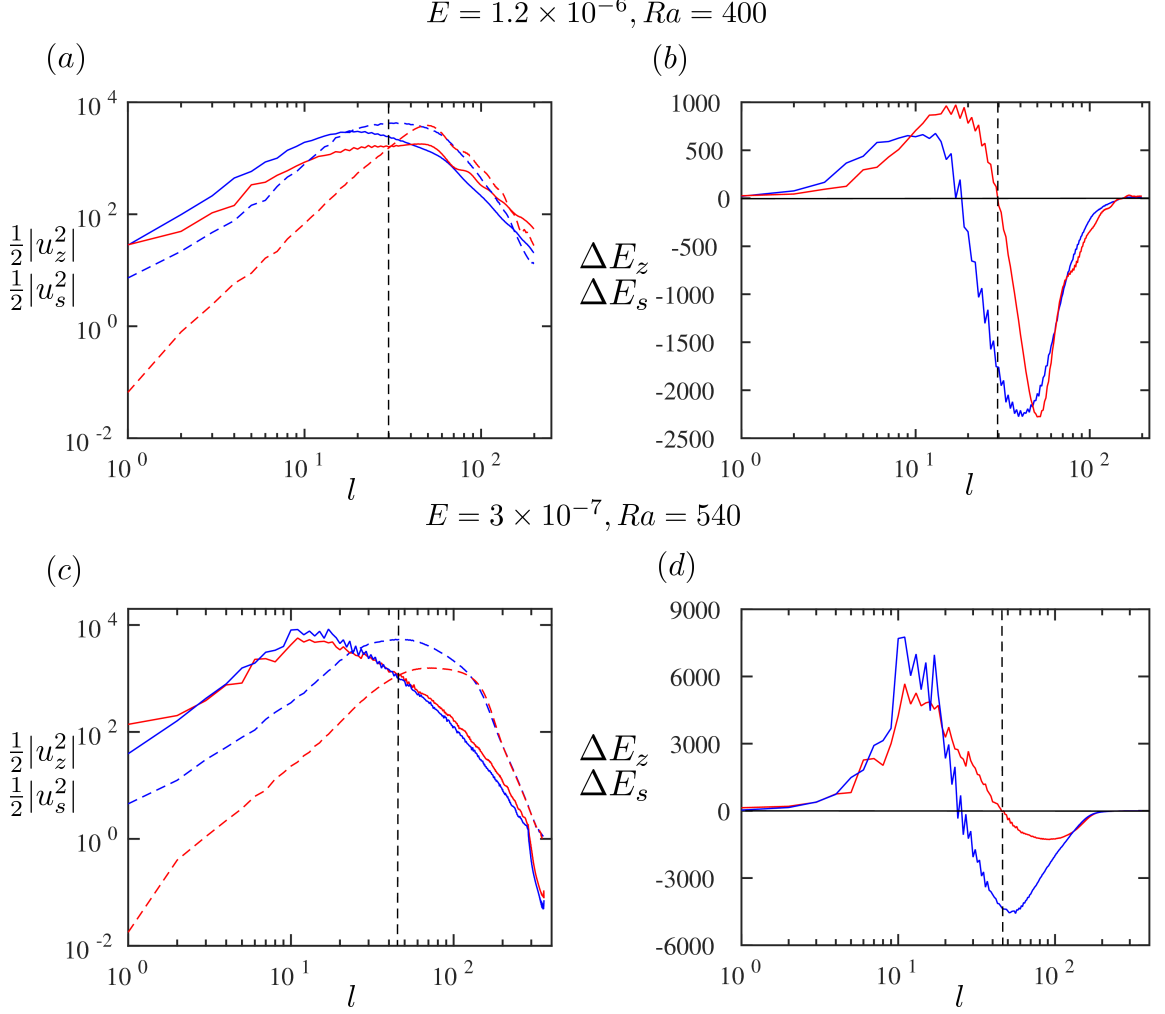


Figure 12: (a) and (c) show time averaged of  $z$ -kinetic energy (red) and  $s$ -kinetic energy (blue) spectra over harmonic degree  $l$  for nonlinear and non-magnetic simulations at two different  $E$ . Solid line is for nonlinear dynamo simulation and dotted line is for non-magnetic simulation. The vertical dotted line shows where  $z$ -kinetic energy of nonlinear simulation falling below nonmagnetic simulation. (b) and (s) show the differences in magnitude of  $z$ -kinetic energy (solid red line) and  $s$ -kinetic energy (solid blue line) between nonlinear and non-magnetic simulation over  $l$ . For  $E = 1.2 \times 10^{-6}$ , the vertical line is at  $l = 30$  and for  $E = 3 \times 10^{-7}$ , the vertical line is at  $l = 46$ .

our results suggests that Lorentz effect the flow much before the saturation. Though how the dynamo models enter into nonlinear equilibrium state is not well understood at present. This requires further regressive study to answer the fundamental questions of turbulent dynamo models. There are few mathematical models, like  $\alpha$ -queching

mechanism [25] or suppression of Lagrangian chaos of the flow [26], which shed some light on it. Though, there has been no specific mathematical models to answer it for a convection driven turbulent dynamo models. It is known that for  $\Lambda \sim \mathcal{O}(1)$ , Magnetic-Archimedian-Coriolis (known as, MAC) force balance holds in a saturated state [27].

However in this study our aim is to show the effect of Lorentz force much earlier than saturation. We look into  $u_z$  at different time instant in the growing phase of the nonlinear dynamo model. Fig. 13 shows three snapshots of isosurfaces  $u_z$  in spherical shell at two spectra range (top panel -  $l \leq 30$  and bottom panel -  $l > 30$ ) for  $E = 1.2 \times 10^{-6}$ . The last snapshots are taken during the growth phase of the magnetic field. Top panel shows that as time progress there is generation of convection outside the TC which is quiescent otherwise in the absence of the magnetic field. This implies that the Lorentz force enhances the convection, which in turn further amplifies the magnetic field in the context of a self-sustained dynamo model. This effect is a hallmark of large scale dipolar magnetic field, (in dynamo model it is axial dipole) which enhances the columnar flow [28]. However in the bottom panel shows decrease in amplitude of  $u_z$  with time. This effect resembles transfer of magnetic energy from kinetic energy the field grows, which is a classical MHD results and the basis of dynamo action [29].

Therefore we look into energy transfer by the Lorentz force in the  $s$  and  $z$ -momentum equations. Two types of Lorentz force consider here - Lorentz force based on axial dipole and nondipole. Lorentz force based on axial dipole is defined as  $(\nabla \times \mathbf{B}_{10}^P) \times \mathbf{B}$  where,  $\mathbf{B}_{10}^P$  is axial dipole and  $\mathbf{B}$  consider the full spectrum. Similar way, nondipole Lorentz force is defined where nondipole component (except axial dipole) consider within the bracket. Energy transfer by Lorentz force is defined as

$$\Sigma_j^i = - \int_V \mathbf{u}_i \cdot [(\nabla \times \mathbf{B}_j) \times \mathbf{B}] dV \quad (15)$$

where  $\Sigma_j^i$  represents volume average transfer over spherical shell of  $i$ -th component of velocity field to  $j$ -th component of magnetic field by Lorentz force [30]. Energy transfers from two different ranges of energy spectra are shown in Fig. 14 based on

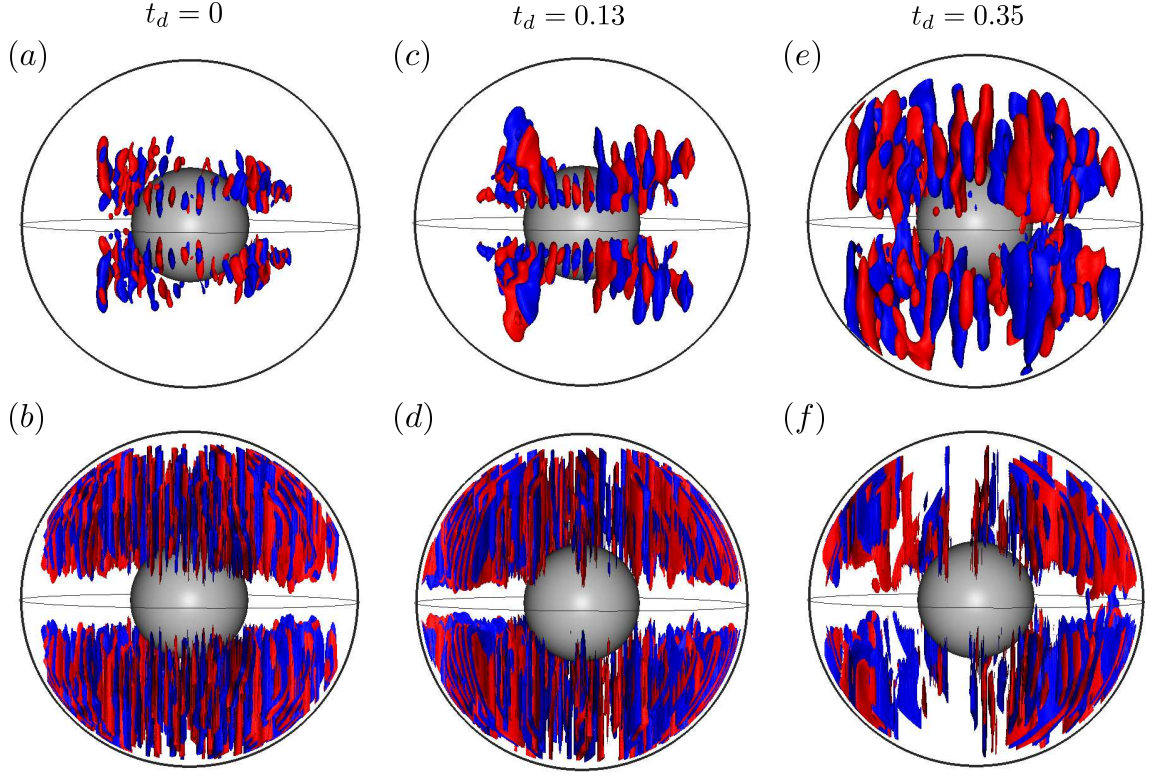


Figure 13: Top panel (*a, c* and *e*) shows isosurface of  $u_z$  (contour levels  $\pm 80$ ) in the range of  $l \leq 30$  for nonlinear simulation at  $E = 1.2 \times 10^{-6}$ ,  $Pr = Pm = 1$ ,  $Ra = 400$ . Bottom panel (*b, d* and *f*) shows isosurface of  $u_z$  (contour levels  $\pm 150$ ) in the range of  $l > 30$  at the same parameters.

two different Lorentz forces. Fig. (*a*) and (*b*) shows energy transfer from velocity (red -  $u_z$ , blue -  $u_s$  and black -  $u_\phi$ ) by axial dipole Lorentz force for  $l \leq 30$  and  $l > 30$ . Notable that energy transfer from  $u_\phi$  is zero in both ranges which means there is no role of  $u_\phi$  in axial dipole generation. Fig. (*a*) suggests that work done by axial dipole Lorentz force in  $u_z$  is positive and for  $u_s$  is negative. This implies that there Lorentz force is taking energy from  $u_z$  and giving to  $u_s$ . Therefore this taking-giving role implies a self-propagation of the axial dipole in a self-sustained dynamo model. However the important note here is that this happens much earlier the saturation, when the magnetic field is weak. Though, the action of Lorentz force on the small scale is comparatively weak as shown in Fig. (*b*). The mean values in the saturated state for  $u_z$  in the range of  $l \leq 30$  and  $l > 30$  are  $6.93 \times 10^7$  and  $6.95 \times 10^5$ . The mean values in the saturated state for  $u_s$  in the range of  $l \leq 30$  and  $l > 30$  are  $-5.41 \times 10^7$

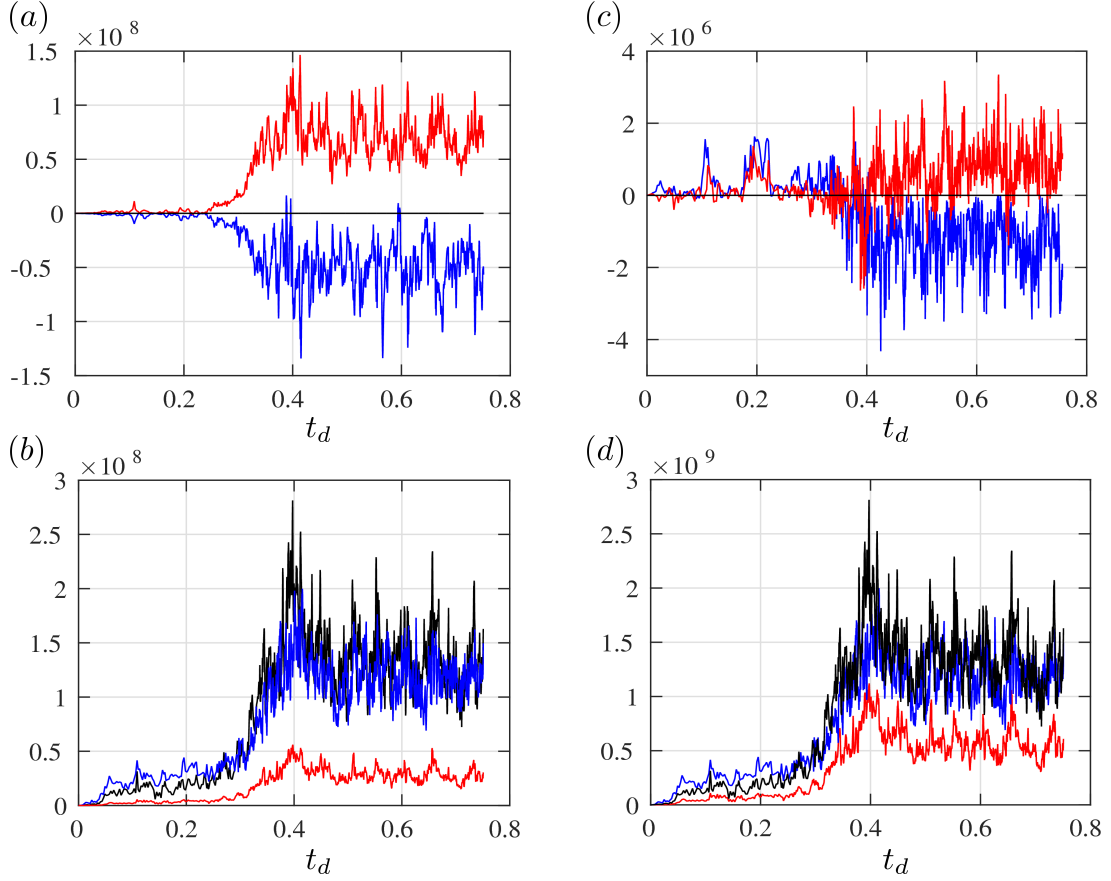


Figure 14: Work done by Lorentz force in the two ranges of  $s$  and  $z$ -kinetic energy spectra. (a and c) represent work done by the Lorentz force based on axial dipole in the nonlinear simulation. (b and d) represent work done by the Lorentz force based on nondipole components. For (a and b) truncated value of  $l$  for the flow is 30. (c and d) shows  $l$  from 30 to  $l_{max} = 220$ . Red line represents energy transfer by Lorentz force from  $u_s$ , blue line represents from  $u_z$  and black line represents from  $u_\phi$ .

and  $-1.45 \times 10^6$ .

### 3.2.2. Helicity generation and preferences in axial dipole magnetic field

The effect of Lorentz force on the flow in a nonlinear dynamo model can be understood by looking at the helicity distribution as shown in rapidly rotating linear magnetoconvection in spherical shell by previous study [28]. The authors imposed a large scale azimuthal magnetic field and find an enhancement of  $z$ -helicity in case of imposed dipolar magnetic field over a quadrupolar field under rapidly rotation, although strength of the field is small. This happens due to the fact that the Lorentz

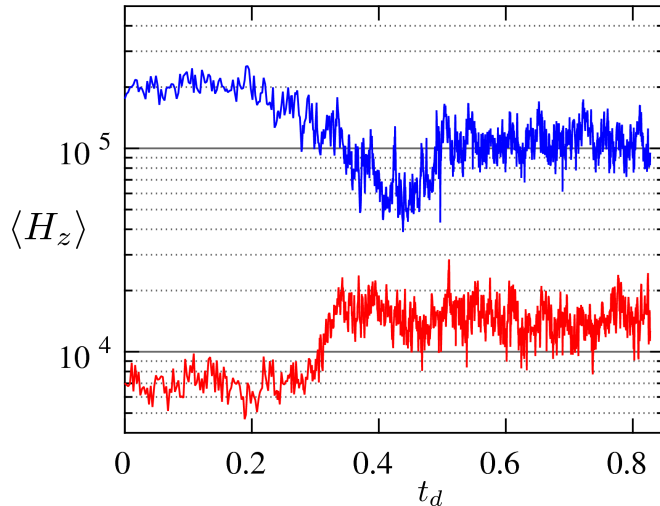


Figure 15: Evolution of volume averaged of  $z$ -helicity ( $\langle H_z \rangle$ ) over southern hemisphere with time. Red line represents  $\langle H_z \rangle$  in the range of  $l \leq 30$  and blue line represents  $\langle H_z \rangle$  in the range of  $l > 30$  for nonlinear simulation at  $E = 1.2 \times 10^{-6}$ ,  $Pr = Pm = 1$ ,  $Ra = 400$ .

force enhance the columnar flow by breaking Taylor-Proudman constrain. However in rapidly rotating dynamo models suggests that the length scale of axisymmetric azimuthal field in the direction of rotation decreases by lowering  $E$  [31]. The authors has shown that by lowering the length scale of the magnetic field, the enhancement of the helicity is getting reduced compare to the non-magnetic case. Therefore care must be taken to make a direct comparison of magnetoconvection studies with nonlinear models. The essenatial difference that comes from magnetoconvection studies that the results are dependent on the initial structure of the imposed field. However the structure of magnetic field in nonlinear models are see too complicated to scale dependent effect of the field on the flow. For that we look into helicity in two different scale of the flow. Fig. 15 shows evolution of the volume averaged  $z$ -helicity (after removing the boundary layer at two boundaries) over northern hemipshere at two different length scales for nonlinear dynamo model at  $E = 1.2 \times 10^{-6}$ . Red line shows  $z$ -helicity of the flow  $l \leq 30$  and blue shows for  $l < 30$ . Overall enhancement of the  $z$ -kinetic helicity with time as magnetic field grows is one of most striking behaviour of the large scale

magnetic field as linear theory predicts. In small large scale we see that  $H_z$  associated with the flow decreases as field grows. The initial and mean value at saturated  $z$ -helicity for  $l \leq 30$  are  $7 \times 10^3$  and  $1.39 \times 10^4$ , respectively. There is almost 2 times of enhancement due to large scale magnetic field. This happens due to the fact that there is a transfer of kinetic energy to magnetic field by the Lorentz force. Fig. 16 shows comparison of time averaged of  $H_z$  between non-magnetic and magnetic simulations for  $l \leq 30$ . Fig. 16 (a) and (d) show isosurface of  $H_z$  in spherical shell at contour level of  $\pm 2 \times 10^4$  for non-magnetic and magnetic case, respectively. For non-magnetic case,  $H_z$  is confined mostly to inner boundary, while in magnetic case  $H_z$  spread over to the outer region. Hence there is an overall enhancement of  $H_z$  as in the range of  $l \leq 30$  as we see in Fig. 15. The middle and bottom panels shows the same plot at two different  $z$ -sections (at  $z = 0.3$  and  $0.6$ ). In the  $z$ -section plot, we see that there is a both positive and negative helicity contribution in the non-magnetic case and while, in magnetic there is a coherent structure of negative helicity present. Fig. 16 shows cyclone and anticyclone for two ranges of  $l$ , which are  $l \leq 30$  and  $l > 30$ . Interestingly, the helicity asymmetry shows up only at  $l > 30$  for the nonlinear dynamo models, while non-magnetic convective models does not shows up any such behaviour. However, the range of  $l \leq 30$ , there is no such asymmetry between cyclone and anticyclone helicity in nonlinear dynamo model, although a overall enhancement is seen compare to non-magnetic case. This behaviour clearly shows the scale dependent behaviour of the magnetic field on the helicity, hence on the flow.

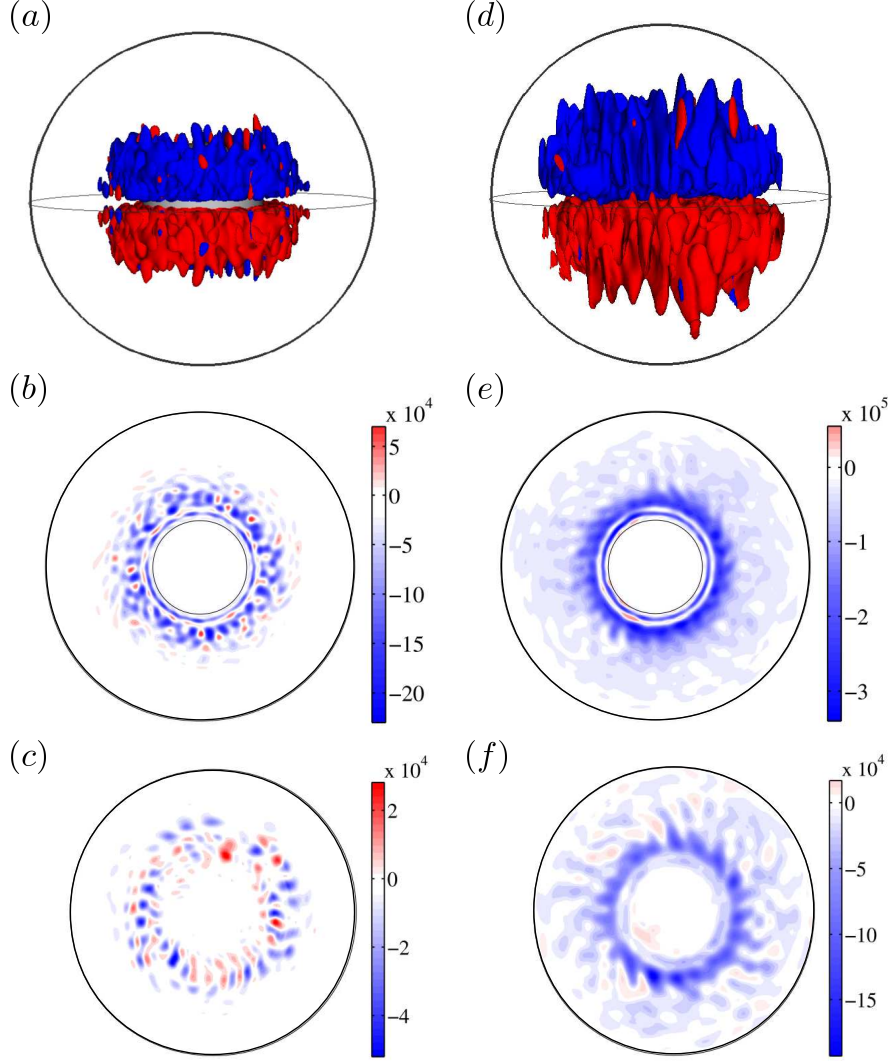


Figure 16: Top panel ( $a$  and  $d$ ) shows isosurface of  $z$ -helicity ( $H_z$ ) (contour levels  $\pm 2 \times 10^4$ ) in the range of  $l \leq 30$  for simulations at  $E = 1.2 \times 10^{-6}$ ,  $Pr = Pm = 1$ ,  $Ra = 400$ . The left panel is for nonmagnetic and right panel is for nonlinear dynamo. Middle panel ( $b$  and  $e$ ) shows  $H_z$  at  $z=0.3$  and bottom panel ( $c$  and  $f$ ) shows  $H_z$  at  $z=0.6$ .

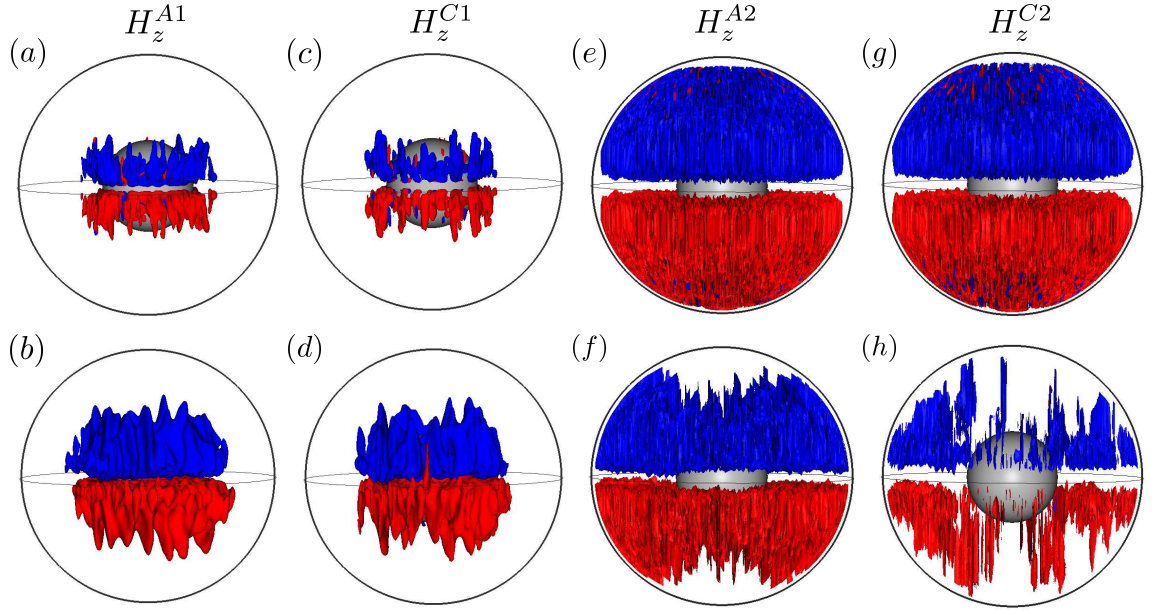


Figure 17: Top panel shows isosurfaces of time averaged of anticyclonic (A) and cyclonic (C)  $z$ -helicity for nonmagnetic simulation and bottom panel shows for nonlinear dynamo simulation at  $E = 1.2 \times 10^{-6}$ ,  $Pr = Pm = 1$ ,  $Ra = 400$ . (a – d) represent in the range of  $l \leq 30$  (contour levels  $\pm 2 \times 10^4$ ) and (e – h) represent in the range of  $l > 30$  (contour levels  $\pm 2 \times 10^5$ ).



#### 4. Discussion and conclusions

In this study we investigate preferences of the axial dipole structure from a seed magnetic field in the rapidly rotating spherical shell dynamo models. We study both nonlinear as well as kinematic regimes. For kinematic models Lorentz force is dropped from the momentum equation. In rapidly rotating system, onset of convection outside the tangent cylinder flow structure appears as an equatorial symmetric. Though by increasing Rayleigh numbers the equatorial symmetric constraint imposed by rotation breaks down. So for that the simulations are done in both low and high Rayleigh numbers.

In low-Ra regime structure of the flow is like an onset of convection. In this case we see that in both nonlinear and kinematic case the dipole structure is preferred and initial magnetic field structure belongs to quadrupole family becomes a failed dynamo. The dipolar magnetic field has an equatorial antisymmetric structure and quadrupolar is equatorial symmetric. As the initial input poloidal magnetic field is very weak, the initial amplification of the magnetic field in the nonlinear simulation is in kinematic regime. In both kinematic and nonlinear dynamos, the fall of the magnetic energy of the quadrupole is effectively a kinematic process since the growth of the field is not much to affect the flow at all. For initial dipole seed field start, both kinematic and nonlinear show a dipolar structure. The analyses suggest that as for quadrupole field, the  $B_\phi$  peaks at the equatorial plane, hence the columnar structure not able to reinforce any poloidal field to the original field as classical- $\alpha$  effect suggests and eventually dynamo fails due to incompleteness of the regeneration cycle. While the columnar structure is able to generate poloidal field from the toroidal field, hence complete the regeneration cycle in the kinematic regime.

Further to test role of the initial magnetic field in polarity selection, we use a mixed seed field composed of majorly axial quadrupole and very little trace of axial dipole (99.99% of  $\Lambda_{20}^P$  and 0.01% of  $\Lambda_{10}^P$ ). In this case the final structure of the magnetic field shows up a dipolar structure. From beginning of the simulation, we see that the axial quadrupole is falling and axial dipole is growing. These results suggest that structure

of the initial magnetic field is playing role in polarity selection.

Since, the input structure of the velocity field is equatorial symmetric under rapid rotation. Therefore to study the role of symmetry of the velocity field in polarity selection, we introduce seed equatorial antisymmetric flow in the low- $Ra$  regime. The results suggest that a successful dipolar dynamo in both kinematic and nonlinear regime from an axial quadrupole seed magnetic field. This happens in the induction equation due to interaction of the equatorial antisymmetric flow with the equatorial symmetric field. Though in high- $Ra$  case, where velocity symmetry break down; there we see a dipole structure of the magnetic field in nonlinear dynamo. Though the kinematic model in this case shows a chaotic solution. Nevertheless, our results suggests that dipole is preferred over quadrupole in all cases of rapidly rotating dynamos. Therefore the preference of the dipole structure in the low- $Ra$  regime is a kinematic effect.

Our second part of the study is preferences of dipole in rapidly rotating dynamo models at high- $Ra$ . Here, emphasise is on to quantify role of the magnetic field in dipole preferences at different strength of the self generated magnetic field by varying Rayleigh numbers. Our focus is on evolution of the field from a axial dipole seed magnetic field in both nonlinear and kinematic regimes.

We look into the  $\mathbf{B}_{20}^T$  generation for two different Rayleigh numbers. Energy analysis suggests that the field is generated by the shearing of axial dipole by differential rotation as the classical  $\omega$ -effect suggests. Energy matrices construct based on Bullard's selection rule give an idea of the interaction between different harmonics of the flow and field to generate the field. For  $Ra = 140$ , we see it is the  $Y_1^0$  of the poloidal field is sheared by  $Y_1^0$  of the toroidal field in both kinematic and nonlinear regime. Though in  $Ra = 220$ , the zonal flow is dominated by a  $Y_3^0$  and energy matrix suggest that in the presence of strong dipole field, the differential rotation which is helping in kinematic regime switch from  $Y_1^0$  to  $Y_3^0$ . Nevertheless, the structure of the differential rotation is still a large scale as classical  $\omega$ -effect shows. We do find that the  $\omega$ -effect is a robust features of a rapidly rotating dynamo.

In the last part of the study we discuss about generation of axial dipole field in

kinematic and nonlinear dynamos. In high- $Ra$  we see effect of the back reaction due to magnetic field by resorting back the dipole structure from a transient chaotic solution before the saturation. Though kinematic dynamo does not show any such behaviour as there is no effect of back reaction on the flow. The important results that has come out from our study is the magnetic field acts on the flow much before the saturation. Our study suggests that the growth of the magnetic field is not a kinematic effect as one might think off, rather a dynamic effect. This dynamic effect grows as the field generated in time and finally brings the saturation. Though we have not study the mechanism of the saturation in this nonlinear models. Strength of the magnetic field in a self sustained dynamos can be done by only varying Rayleigh number (energy input), unlike in magnetoconvection problem. In our model we vary Rayleigh number to see the effect of back reaction on the dynamics. The results suggest that effect of back reaction delays as we decrease the Rayleigh number. In our high- $Ra$  simulations, we find two regimes - the regime before departure between nonlinear and kinematic simulations as kinematic and after (before the saturation) as nonlinear phases. In kinematic phase, we find that classical Parker dynamo model works quite well, though it does not help much in large scale magnetic field (axial dipole) generation. As the model evolves into a nonlinear phase, we do see a sudden growth of axial dipole. Energy and induction terms analyses provide a hint on a different generation mechanism. We find that the term which support the axial dipole in kinematic phase is becoming a negative contributor in the nonlinear phase. The detail analyses suggest that the  $r$ -component of the axial dipole is supported by a advection of gradient of small scale radial magnetic field. Though advection does not contribute to the overall magnetic energy amplification. Transport coefficients of mean field suggests that advection plays a important role in dipole field generation [23] [17].

## References

- [1] M. Kono, P. H. Roberts, Recent geodynamo simulations and observations of the geomagnetic field, *Rev. Geophys.* 40 (2002) 101–113.
- [2] P. H. Roberts, E. M. King, On the genesis of the earth’s magnetism, *Rep. Prog. Phys.* 76 (2013) 55p.
- [3] F. H. Busse, R. D. Simitev, Parameter dependences of convection-driven dynamos in rotating spherical fluid shells, *Geophys. Astrophys. Fluid Dyn.* 100 (2006) 341–361.
- [4] E. Grote, F. H. Busse, A. Tilgner, Convection-driven quadrupolar dynamos in rotating spherical shells, *Physical Review E* 60 (1999) 5025–5028.
- [5] E. Grote, F. H. Busse, A. Tilgner, Regular and chaotic spherical dynamos, *Phys. Earth Planet. Inter.* 117 (2000) 259–272.
- [6] N. Ishihara, S. Kida, Equatorial magnetic field intensification by convection vortices in a rotating spherical shell, *Fluid Dynamic Reserach* 31 (2002) 253–274.
- [7] J. Aubert, J. Wicht, Axial vs. equatorial dipolar dynamo models with implications for planetary magnetic fields, *Earth and Planetary Science Letters* 221 (2004) 409–419.
- [8] C. A. Jones, *Thermal and compositional convection in the outer core*, Elsevier, 2007.
- [9] N. Schaffer, P. Cardin, Quasi-geostrophic kinematic dynamos at low magnetic prandtl number, *Earth and Planetary Science Letters* 245 (2006) 595–604.
- [10] E. Bullard, H. Gellman, Homogeneous dynamos and terrestrial magnetism, *Phil. Trans. R. Soc. Lond. A* 247 (1954) 213–278.
- [11] R. Avalos-Zuniga, F. Plunian, K. H. Radler, Rossby waves and  $\alpha$ -effect, *Geophys. Astrophys. Fluid Dyn.* 103 (2009) 375–396.

- [12] A. P. Willis, D. Gubbins, Kinematic dynamo action in a sphere: effects of periodic time-dependent flows on solutions with axial dipole symmetry, *Geophys. Astrophys. Fluid Dyn.* 96 (2004) 537–554.
- [13] B. Sreenivasan, C. A. Jones, The role of inertia in the evolution of spherical dynamos, *Geophys. J. Int.* 164 (2006) 467–476.
- [14] T. G. Cowling, The magnetic field of sunspots, *MNRAS* 94 (1934) 39–48.
- [15] D. Gubbins, K. Zhang, Symmetry properties of the dynamo equations for palaeomagnetism and geomagnetism, *Phys. Earth Planet. Inter.* 75 (1993) 225–241.
- [16] E. N. Parker, Hydromagnetic dynamo models, *Astrophys. J.* 122 (1955) 293–314.
- [17] M. Schinner, L. Petitdemange, E. Dormy, Dipole collapse and dynamo waves in global direct numerical simulations, *Astrophys. J.* 752:121 (2012) 1–12.
- [18] J. Aubert, Steady zonal flows in spherical shell dynamos, *J. Fluid Mech.* 542 (2005) 53–67.
- [19] M. Steenbeck, F. Krause, K. H. Radler, A calculation of the mean electromotive force in an electrically conducting fluid in turbulent motion under the influence of coriolis forces, *Zeitschr.Naturf. Teil A* 21 (1966) 369–376.
- [20] H. K. Moffatt, *Magnetic Field Generation in Electrically Conducting Fluids*, Cambridge University Press, London, 1978.
- [21] M. Schinner, K. H. Radler, D. Schmitt, M. Rheinhardt, U. R. Christensen, Mean-field view on rotating magnetoconvection and a geodynamo model, *Astron. Nachr.* 326 (2005) 245–249.
- [22] M. Schinner, K. H. Radler, D. Schmitt, M. Rheinhardt, U. R. Christensen, Mean-field view on geodynamo models, *Magnetohydrodynamics* 42 (2006) 111–122.

- [23] M. Schinner, K. H. Radler, D. Schmitt, M. Rheinhardt, U. R. Christensen, Mean-field concept and direct numerical simulations of rotating magnetoconvection and the geodynamo, *Geophys. Astrophys. Fluid Dyn.* 101 (2007) 81–116.
- [24] A. M. Soward, Convection driven dynamos, *Phys. Earth Planet. Inter.* 20 (1979) 134–151.
- [25] G. Rudiger, K. L. L., Alpha effect and alpha-quenching, *Astron. Astrophys.* 269 (1993) 581–588.
- [26] F. Cattaneo, D. W. Hughes, E. Kim, Suppression of chaos in a simplified nonlinear dynamo model, *Phys. Rev. Lett.* 76 (1996) 2057–2060.
- [27] J. B. Taylor, The magneto-hydrodynamics of a rotating fluid and the earth’s dynamo problem, *Proc. R. Soc. Lond.* 274 (1963) 274–283.
- [28] B. Sreenivasan, C. A. Jones, Helicity generation and subcritical behaviour in rapidly rotating dynamos, *J. Fluid Mech.* 103 (2011) 1–26.
- [29] P. A. Davidson, *An Introduction to Magnetohydrodynamics*, Cambridge University Press, New York, 2001.
- [30] F. Takahashi, H. Shimizu, A detailed analysis of a dynamo mechanism in a rapidly rotating spherical shell, *J. Fluid Mech.* 70 (2012) 228–250.
- [31] V. Gopinath, B. Sreenivasan, On the control of rapidly rotating convection by an axially varying magnetic field, *Geophys. Astrophys. Fluid Dyn.* 109 (2015) 567–586.

## Appendix A Bullard’s selection rule

Eq. 5 can be written as

$$\mathbf{u} = \sum_{m=0}^M \sum_{l=1}^L (\mathbf{u}_{lm}^{Tc} + \mathbf{u}_{lm}^{Ts} + \mathbf{u}_{lm}^{Pc} + \mathbf{u}_{lm}^{Ps}) \quad (\text{A.1})$$

where, the vector harmonics are given as, for example

$$\begin{aligned}\mathbf{u}_{lm}^{Tc} &= \nabla \times \nabla \times [u_{lm}^{Tc}(r)Y_l^m(\theta) \cos \phi \hat{\mathbf{r}}] \\ \mathbf{u}_{lm}^{Ts} &= \nabla \times \nabla \times [u_{lm}^{Ts}(r)Y_l^m(\theta) \sin \phi \hat{\mathbf{r}}]\end{aligned}\tag{A.2}$$

Similar way, we can expand the  $\mathbf{B}$ .

#### A.1 Rules for $\mathbf{B}_{10}^P$ and $\mathbf{B}_{20}^P$ generation

##### A.1.1 For combinations of $(\mathbf{u}^P \mathbf{B}^P \mathbf{B}^P)$

The first two terms inside bracket denotes flow and magnetic field of the induction term and last term represents the induced field. Superscripts  $P$  and  $T$  denote toroidal and poloidal components of the vector field, respectively. Degree of the vectors are defined as  $l_\alpha$ ,  $l_\beta$  and  $l_\gamma$  and orders are as  $m_\alpha$ ,  $m_\beta$  and  $m_\gamma$  according to their appearance inside the bracket. Note that our notation of degrees are different from the Bullard's notation [10].

###### (a) Rules for $m_\alpha$ and $m_\beta$

According to the selection rule for generating axisymmetric field both inducing flow and field will share common value of order i.e.,  $m_\alpha = m_\beta$ . This rule is valid for any toroidal and poloidal combinations of flow and field.

###### (b) Rules for $l_\alpha$ and $l_\beta$

The restriction for degrees are  $l_\alpha + l_\beta + l_\gamma$  is even and they can form the sides of a triangle (degenerate case are  $l_\alpha = l_\beta + l_\gamma$ , etc ) means  $|l_\alpha - l_\gamma| \leq l_\beta \leq (l_\alpha + l_\gamma)$ .

Therefore, for generating  $\mathbf{B}_{10}^P$  i.e., by fixing ( $l_\gamma = 1$ ), range of  $l_\beta$  is between  $(l_\alpha - 1)$  and  $(l_\alpha + 1)$ . So the combinations are [1, 2], [2, 1], [2, 3], [3, 2], [3, 4], etc, where first digit shows  $l_\alpha$  and second shows  $l_\beta$ .

Similarly, for generating  $\mathbf{B}_{20}^P$  i.e., by fixing ( $l_\gamma = 2$ ), the possible combinations of  $l_\alpha$  and  $l_\beta$  are [1, 1], [1, 3], [2, 2], [2, 4], etc.

##### A.1.2 For combinations of $(\mathbf{u}^P \mathbf{B}^T \mathbf{B}^P)$ and $(\mathbf{u}^T \mathbf{B}^P \mathbf{B}^P)$

###### (a) Rules for $m_\alpha$ and $m_\beta$

Rule of A.1.1 (a) holds for this combinations.

(b) Rules for  $l_\alpha$  and  $l_\beta$

The range of  $l$  are same as A.1.1 (b) except,  $l_\alpha + l_\beta + l_\gamma$  is odd and two harmonics should not be identical. The latter suggests that for example, for a particular choices of combinations of  $\mathbf{u}_{lm}^{Tc}$  and  $\mathbf{B}_{lm}^{Tc}$ , or  $\mathbf{u}_{lm}^{Ps}$  and  $\mathbf{B}_{lm}^{Ps}$  can not generate any poloidal magnetic field. So for generating  $\mathbf{B}_{10}^P$ , the combinations of  $l_\alpha$  and  $l_\beta$  are  $[1, 1]$ ,  $[2, 2]$ ,  $[3, 3]$ ,  $[4, 4]$ , etc (Note that, two harmonics should not be identical but they can share same  $l$  and  $m$ ). The combinations of  $l_\alpha$  and  $l_\beta$  for  $\mathbf{B}_{20}^P$  are  $[1, 2]$ ,  $[1, 3]$ ,  $[2, 1]$ ,  $[2, 3]$ , etc.

## A.2 Rules for $\mathbf{B}_{20}^T$ generation

### A.2.1 For combinations of $(\mathbf{u}^P \mathbf{B}^T \mathbf{B}^T)$ and $(\mathbf{u}^T \mathbf{B}^P \mathbf{B}^T)$

(a) Rules for  $m_\alpha$  and  $m_\beta$

Rule of A.1.1 (a) holds for this combinations.

(b) Rules for  $l_\alpha$  and  $l_\beta$

The range of  $l$ s are same as A.1.1 (b). The combinations of  $l_\alpha$  and  $l_\beta$  for  $\mathbf{B}_{20}^T$  are  $[1, 1]$ ,  $[1, 3]$ ,  $[2, 2]$ ,  $[2, 4]$ , etc.

### A.2.2 For combinations of $(\mathbf{u}^P \mathbf{B}^P \mathbf{B}^T)$ and $(\mathbf{u}^T \mathbf{B}^T \mathbf{B}^T)$

(a) Rules for  $m_\alpha$  and  $m_\beta$

Rule of A.1.1 (a) holds for this combinations.

(b) Rules for  $l_\alpha$  and  $l_\beta$

The range of  $l$ s are same as A.1.2 (b). The combinations of  $l_\alpha$  and  $l_\beta$  for  $\mathbf{B}_{20}^T$  are  $[1, 2]$ ,  $[2, 1]$ ,  $[2, 3]$ ,  $[2, 3]$ , etc.